Thermodynamic coupling in the computation of dendrite growth kinetics for multicomponent alloys

Gildas Guillemot, Oriane Senninger, Christopher Hareland, Peter Voorhees, Charles-André Gandin

To cite this version:

Gildas Guillemot, Oriane Senninger, Christopher Hareland, Peter Voorhees, Charles-André Gandin. Thermodynamic coupling in the computation of dendrite growth kinetics for multicomponent alloys. Calphad, 2022, 77, pp.102429. 10.1016/j.calphad.2022.102429 . hal-03838017

HAL Id: hal-03838017
https://hal.science/hal-03838017v1

Submitted on 3 Nov 2022

Thermodynamic coupling in the computation of dendrite growth kinetics for multicomponent alloys

Gildas Guillemot[a,*], Oriane Senninger[a], Christopher A. Hareland[b],
Peter W. Voorhees[b], Charles-André Gandin[a]

[a] *MINES ParisTech, PSL University, CEMEF UMR CNRS 7635, CS10207, 06904 Sophia Antipolis, France*
[b] *Department of Materials Science and Engineering, Northwestern University, 2220 Campus Drive, Evanston, IL 60208, USA*

Abstract

The growth kinetics of a dendrite tip are of paramount importance for microstructure modeling in materials science and engineering. However, theories for multicomponent alloys are limited, primarily due to approximations in the relevant thermodynamic data. The present contribution first reports on a pragmatic implementation of a general framework coupled with thermodynamic equilibrium calculations. It is applied to the widely used IN718 nickel-base superalloy. Discussions on the output of the model are based on comparisons with the commonly found approximations for multicomponent alloys. Finally, the remaining issues to reach applications at high growth rates are given, paving the way for future developments.

Keywords: Solidification, Dendrite tip, Growth kinetics, Thermodynamic coupling

---

1. Introduction

In solidification processing, a large variety of microstructures can form from the melt. When a single solid phase is growing, it is referred to as dendritic, although planar and cellular morphologies are also seen [1, 2, 3, 4]. The dendritic microstructure influences the final properties of metallic parts. It is consequently of prime importance to master its development and length scales so as to satisfy the requirements for the targeted end-use applications.

At large temperature gradients, directional solidification is commonly observed, giving rise to constrained growth and elongated columnar grains. Columnar grains are observed in most industrial processes involving solidification such as casting, welding and additive manufacturing [2], hence covering a wide range of cooling rates. Tiller *et al.* [5] first established the constitutional supercooling criterion that defines a condition for the stability of a planar front growing in a temperature gradient, G, at constant velocity, v, with solute redistribution taking place at the solid-liquid interface. Assuming steady state, the criterion states that the length scale for solute diffusion in the liquid, D/v, should remain higher than the length scale associated to the temperature gradient, $\Delta T_0/G$, where D and ΔT_0 are the diffusion coefficient of the solute specie in the liquid and the solidification interval, respectively. In other

---

[*] Corresponding author
Email address: `Gildas.Guillemot@mines-paristech.fr` (Gildas Guillemot)

words, if the velocity is higher than the critical value $v_c = D\,G/\Delta T_0$, the front becomes unstable. At higher velocity, Mullins and Sekerka [6] developed a stability analysis. They found that the interface can restabilize if a capillary length, $\Gamma k/\Delta T_0$, becomes larger than the diffusion length scale, where Γ and k are the Gibbs-Thomson coefficient defined at the solid-liquid interface and the segregation or partition coefficient of the solute specie, respectively. The so-called absolute stability limit is then defined by the absolute velocity, $v_a = D\,\Delta T_0/(k\,\Gamma)$, above which the interface remains planar. It is worth noting that the stability analysis was further extended by Trivedi and Kurz to cover the effect of different temperature gradients in the liquid and solid phases [7]. Additionally, Coates *et al.* [8] and Bobadilla *et al.* [9] proposed stability analyses for dilute multicomponent alloys. However, the foundational work proposing a generalized formalism that includes cross-diffusion of solute species in the liquid phase was first presented by Hunziker [10].

Literature reflects a longstanding interest in dendritic growth [3, 4]. The preliminary experimental observations of Papapetrou [11] established that the dendrite tip shape is well-approximated by a paraboloid of revolution. This hypothesis offers the advantage of simplifying the solution of the conservation equation in the liquid upon steady growth. Ivantsov provided the solution of the diffusion problem for heat ahead of an isothermal paraboloidal dendrite developing into an infinite reservoir of liquid maintained at a fixed temperature [12]. Upon constrained growth and for alloys, diffusion of solute species is the dominant phenomenon. At the tip of the paraboloidal dendrite, the chemical supersaturation, $\Omega = (w^{ls} - w_0)/(w^{ls} - w^{sl})$, relates to the Péclet number, $Pe = r\,v/(2\,D)$, where w^{ls} and w^{sl} are the composition at the solid-liquid interface in the liquid and in the solid, respectively, and w_0 is the far-field composition in the liquid, equal to the nominal alloy composition. The Péclet number is thus the ratio of the tip radius, r, over the diffusive length scale $2\,D/v$. Again, the extension for a multicomponent alloy including cross-diffusion of solute species in the liquid was given by Hunziker [10].

The above solution of the diffusion problem is not sufficient to independently solve for the tip radius when fixing the velocity, or vice-versa [3, 4, 13], and only gives access to its product, $r\,v$, through the Péclet number when fixing the supersaturation. Note that upon directional solidification, the latter can be related to the tip temperature when assuming thermodynamic equilibrium at the solid-liquid interface. The preliminary hypothesis assuming that dendrites develop at their maximum velocity [14, 15, 16] could not retrieve experimental observations reported by Glicksman *et al.* [17, 18], which revealed a larger curvature radius and lower growth velocity. Langer and Müller-Krümbhaar [19] proposed the marginal stability criterion, assuming that the dendrite tip develops with a radius close to the minimum wavelength at which instabilities develop on a planar interface, λ_{min}, previously calculated by Mullins and Sekerka [6]. This latter choice was associated to a selection constant, $\sigma^* = (2\pi)^{-2}$. The operating point of a steady constrained dendrite tip that associates both the Ivantsov solution and the stability criterion with the selection constant σ^* was then delivered by Kurz *et al.* [20]. It also included a linear approximation of the effects of interface curvature on the thermodynamic equilibrium and the effect of solute trapping following the model developed by Aziz [21] for an ideal dilute binary alloy. Finally, the microsolvability theory [22, 23, 24, 25] emerged, using a constant ratio $(r/\lambda_{min})^2 = \sigma^*/\sigma$, where σ is a selection constant parameter and a function of the interface energy anisotropy that can depart from the marginal stability criterion parameter σ^*. The above set of equations were recognized as a suitable modelling framework for the study of a steady growing dendrite under a purely diffusive regime.

Models of dendrite growth kinetics for multicomponent alloys remain scarce in the literature despite a clear industrial interest, as alloys are generally composed of several chemical species, each of specific interest to control the final properties. A common approach consists of defining a pseudo-binary system based on the physical and thermodynamic properties of each solute [26, 27]. A multilinear phase diagram is also proposed [8, 9], which estimates thermodynamic equilibrium properties at the liquidus of the alloy and/or extracts temperature-dependent liquidus and solidus curves from the binary phase diagrams between the solvent and each solute specie [28]. Some authors have proposed extensions of the above framework by coupling with the Calphad method [29, 30] or using the Hunziker theory with a full matrix of the diffusion coefficients in the liquid, and have compared the calculations to the results of high-velocity experiments [31]. Lahiri and Choudhury [32] and Liu *et al.* [33] recently discussed the outputs of phase-field simulations of dendritic growth with a theory for a multicomponent alloy. However, a model of dendrite growth kinetics for multicomponent alloys that includes systematic coupling with thermodynamic data and its application to complicated multicomponent alloys (beyond ternary systems) is clearly lacking. Here, we propose an extension of the model by Hunziker [10] coupled with thermodynamic equilibrium calculations including interface curvature and diffusion matrix evaluation. First, the model and solution algorithm are described. Then, a calculation is presented for the dendrite tip kinetics of IN718, an eight-component nickel-base superalloy that is widely used in casting and additive manufacturing of component for high temperature applications. The last part of the paper compares the results of the general present model with the common approximations reported in the literature, and identifies potential further developments.

2. Modeling

2.1. Theory

We consider hereafter a solid paraboloidal dendrite, s, growing in a reservoir of liquid, l, at the nominal composition of the alloy, $\mathbf{w^0} = (w_i^0)_{1\leq i\leq N}$ in mass fractions, defined for the N chemical species of a multicomponent alloy. Index N is associated with the solvent (main component) and indices i ($1 \leq i \leq N-1$) with the solutes (alloying components). The densities of the solid and liquid phases are assumed constant and equal, hereafter denoted by ρ, and convection phenomena are ignored. The dendrite is assumed to grow steadily with its main axis aligned with the z-axis direction, i.e., with stable velocity, $\mathbf{v} = v\,\mathbf{z}$, and curvature radius at its tip, r, in well-established composition fields. Similarly, a fixed temperature gradient of uniform magnitude, G, in both the solid and liquid phases, is imposed along the z-axis direction, $\mathbf{G} = G\ \mathbf{z}$. Fig. 1 schematizes the solid paraboloidal dendrite tip and the profiles for two solute species in the liquid. Solute diffusion is neglected in the solid phase, and dendrite growth is solely driven by diffusion in the liquid phase. Cross-diffusion effects in the liquid phase take place assuming a constant diffusion matrix, $\mathbf{D} = (D_{ij})_{1\leq(i,j)\leq N-1}$ evaluated at the liquidus temperature, T_L, and at the nominal composition of the alloy, i.e. $\mathbf{D}(\mathbf{w^0}, T_L)$. The diffusion coefficients in the liquid, D_{ij}, links the contribution of the composition gradient of the solute species j in the liquid at the solid-liquid interface, $\nabla(\rho\, w_j)$, to the diffusion flux of the solute species i, $J_i = -\sum_{j=1}^{N-1} D_{ij}\nabla(\rho\, w_j)$.

The diffusion matrix can include non-zero off-diagonal terms, allowing the possibility of forming concentration profiles in the liquid that do not monotonically increase or decrease, yet recover the nominal alloy composition far away from the interface, as illustrated by w_2 in Fig. 1. Note that the present hypotheses are the same as in Hunziker's theory [10], which also includes an isothermal dendrite tip, T, and an isotropic interface energy, γ, when deriving the extension of the Ivantsov solution to multicomponent alloys [12] and the stability analysis of a solid-liquid planar front [6]. Additionally, under the assumption of thermodynamic equilibrium at the solid-liquid interface, the interface compositions in the solid, w_i^{sl}, and in the liquid, w_i^{ls}, for all components i, $1 \leq i \leq N-1$, are given by a tie line of the phase diagram at the tip temperature, T, also defining the partitioning of the solute species between the solid and liquid phases with the segregation coefficient, $k_i = w_i^{sl}/w_i^{ls}$.

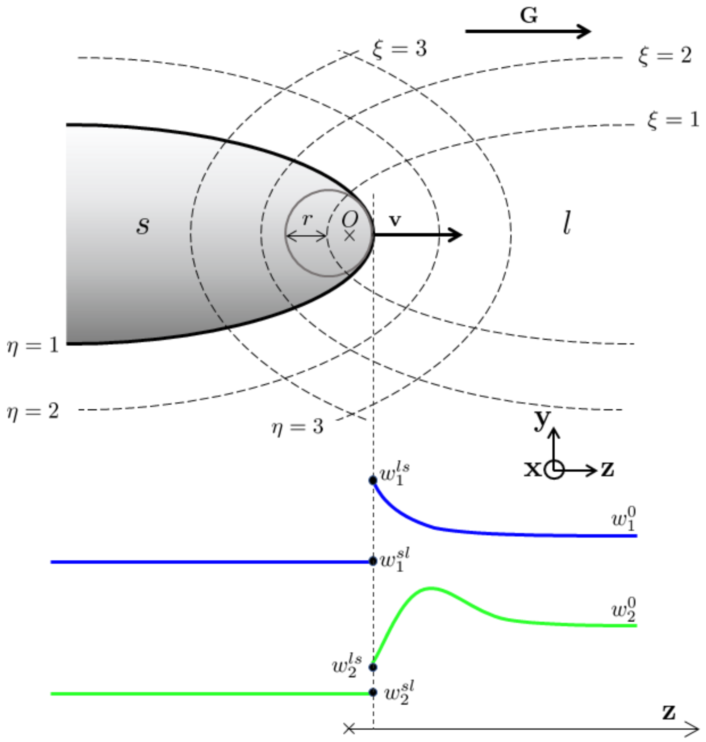

Figure 1: Schematic drawings of (grey) a paraboloidal solid dendrite, s, growing in a liquid phase, l, with tip velocity $\mathbf{v} = v\,\mathbf{z}$, the origin O of the $(\mathbf{x}, \mathbf{y}, \mathbf{z})$ reference frame being located in the solid, along the main axis of the paraboloidal dendrite ($\eta = 0$), at distance from the interface equal to half the radius of the sphere defining the tip radius, r. A constant and uniform temperature gradient, $\mathbf{G} = G\,\mathbf{z}$, is imposed to the entire domain. Steady composition profiles for solute components numbered (blue) 1 and (green) 2 are sketched along the z-axis with progressive evolution in the liquid towards their respective nominal composition, w_1^0 and w_2^0, far away from the solid-liquid interface. The paraboloidal coordinates defined by $\eta^2 = (z + \sqrt{x^2+y^2+z^2})/r$ and $\xi^2 = \eta^2 - 2\,z/r$ are represented as dashed lines.

- *Solute diffusion*

The composition field in the liquid surrounding the steady growing dendrite tip for any solute species is given by the solution of the solute mass-conservation equation. Using the paraboloidal coordinate η defined in Fig. 1, the general solution for solute species i, $w_i(\eta)$ $(1 \leq i \leq N-1)$, depends on the eigenvalues of the diffusion matrix, $\mathbf{B} = (B_i)_{1\leq i\leq N-1}$, the transformation matrix made of the unit eigenvectors $\mathbf{U}_{.,j}$, $\mathbf{U} = (U_{ij})_{1\leq (i,j)\leq N-1}$, of the diffusion matrix, $\mathbf{D}$, and the Péclet numbers of the dendrite tip associated to the eigenvalues, $\mathbf{Pe} = (Pe_i)_{1\leq i\leq N-1}$ with $Pe_i = (r\,v)/(2\,B_i)$ [10]:

$$w_i(\eta) = w_i^0 + \sum_{j=1}^{N-1} C_j U_{ij} \frac{\mathrm{E}_1(Pe_j \eta^2)}{\mathrm{E}_1(Pe_j)} \tag{1}$$

where E_1 is the exponential integral function [34]. The unknown parameters C_j are the magnitudes of the solutions associated to the eigenvectors and eigenvalues. They can be calculated from the compositions at the solid-liquid interface, $\eta = 1$, as follows. From Eq. (1), one can derive the conservation equation at the interface for any solute component i:

$$w_i^{ls} - w_i^{sl} = \sum_{j=1}^{N-1} \frac{C_j\,U_{ij}}{\mathrm{Iv}(Pe_j)} \tag{2}$$

where $\mathrm{Iv(x)} = x\exp(x)\,\mathrm{E}_1(x)$ is the Ivantsov function [12]. It is worth noting that assuming a constant interfacial composition is equivalent to approximating the interfacial temperature and curvature as constants, as discussed in reference [10]. The C_j coefficients can then be estimated from Eq. (2) by inverting the $\mathbf{U}$ matrix, giving $C_j = \sum_{k=1}^{N-1} U_{jk}^{-1}\,\mathrm{Iv}(Pe_j)\,(w_k^{ls} - w_k^{sl})$. Eq. (1) then becomes

$$w_i(\eta) = w_i^0 + \sum_{j=1}^{N-1}\sum_{k=1}^{N-1} (w_k^{ls} - w_k^{sl})\,U_{ij}\,U_{jk}^{-1}\,\mathrm{Iv}(Pe_j) \frac{\mathrm{E}_1(Pe_j\,\eta^2)}{\mathrm{E}_1(Pe_j)} \tag{3}$$

At the solid-liquid interface, $\eta = 1$ (or $z = r/2$), Eq. (3) simplifies to the following relation between the set of interfacial compositions in the liquid, $\mathbf{w}^{ls} = (w_i^{ls})_{1\leq i\leq N-1}$, the far-field compositions in the liquid, $\mathbf{w}^0$, and the Péclet numbers of the dendrite tip defined by eigenvalues:

$$w_i^{ls} = w_i^0 + \sum_{j=1}^{N-1}\sum_{k=1}^{N-1} \left(w_k^{ls} - w_k^{sl}\right)\,U_{ij}\,U_{jk}^{-1}\,\mathrm{Iv}(Pe_j) \tag{4}$$

When cross-diffusion is neglected, $\mathbf{D}$ becomes a diagonal matrix given by $\mathbf{D} = (D_{ij}\,\delta_{ij})_{1\leq (i,j)\leq N-1}$, where $\delta_{..}$ is the Kronecker delta. This leads to $\mathrm{U} = \mathrm{U}^{-1} = \mathbf{I}$, the identity matrix. Consequently, $B_i = D_i$ and $Pe_i = (r\,v)/(2\,D_i)$ for any i $(1 \leq i \leq N-1)$. This reduces Eq. (4) to the conventional Ivantsov relation, which links the Péclet number for any element to its chemical supersaturation, $\Omega_i = (w_i^{ls} - w_i^0)/(w_i^{ls} - w_i^{sl})$.

- *Stability criterion*

At a given velocity, v, within the possible interval of interface instability, $v_c \leq v \leq v_a$, a stability analysis shows the existence of a range of perturbation wavelengths, λ, corresponding to wavenumber, $\omega = 2\pi/\lambda$. The marginal stability criterion states that the minimum wavelength for instability, λ_{min}, can be used to estimate the dendrite tip radius, r [19]. Determining this wavelength requires finding the solution of the equation that expresses the time derivative of the amplitude of the perturbation, equivalent to [6, 10]:

$$\sum_{i=1}^{N-1} m_i \sum_{j=1}^{N-1} U_{ij} F_j - \Gamma \omega^2 - G = 0 \tag{5}$$

where the liquidus slope, m_i, is defined for solute species i as:

$$m_i = \left. \frac{\partial T}{\partial w_i^{ls}} \right|_{w_{j \neq i}^{ls}} \tag{6}$$

Γ is the Gibbs-Thomson coefficient, which can be deduced from the curvature undercooling as detailed hereafter. The set of $\mathbf{F} = (F_i)_{1 \leq i \leq N-1}$ coefficients are deduced from the compatibility of the temperature and composition fields following the methodology derived by Hunziker [10]. Simplifications and rewriting yields[1] for all k elements $(1 \leq k \leq N-1)$:

$$\sum_{j=1}^{N-1} \left[U_{kj}\, \zeta_j - 2 \sum_{i=1}^{N-1} U_{ij}\, K_{ki} \right] F_j = - \sum_{j=1}^{N-1} v \, \frac{U_{kj}\, A_j}{B_j} \zeta_j \tag{7}$$

where ζ_i parameters are related to velocity and defined for any index i considering the eigenvalues B_i:

$$\zeta_i = 1 - \sqrt{1 + \left(\frac{2 \omega B_i}{v} \right)^2} \tag{8}$$

The $\mathbf{A} = (A_i)_{1 \leq i \leq N-1}$ vector in Eq. (7) is expressed as a function of the difference between interface compositions, $\mathbf{\Delta w} = \mathbf{w}^{ls} - \mathbf{w}^{sl} = (w_i^{ls} - w_i^{sl})_{1 \leq i \leq N-1}$:

$$\mathbf{A} = \mathbf{U^{-1}} \cdot \mathbf{\Delta w} \tag{9}$$

The K coefficients in Eq. (7) comprise the partition matrix $\mathbf{K} = (K_{ij})_{1 \leq (i\,,j) \leq N-1}$, which represents the effect of liquid composition changes on solid compositions from the relevant tie-lines of the phase diagram. The coefficients are defined from the derivative of the interface compositions at the dendrite tip, $\mathbf{w}^{sl}$, as:

$$K_{ij} = \left. \frac{\partial w_i^{sl}}{\partial w_j^{ls}} \right|_{w_{k \neq j}^{ls}} \tag{10}$$

These K_{ij} coefficients are estimated along the liquidus surface, and the derivative is evaluated while fixing every composition in the liquid phase other than the j component, $w_{k \neq j}^{ls}$, and with no condition imposed on the solid composition, w_i^{sl}, nor on the temperature, T. Note that the diagonal terms, $K_{ii} = \partial w_i^{sl} / \partial w_i^{ls} |_{w_{k \neq i}^{ls}}$, are not necessarily equal to the partition coefficients, k_i. This could be the case for a linearized phase diagram, i.e., with constant slopes of the liquidus and solidus surfaces as well as constant partition coefficients. This was the case for the applications developed by Hunziker [10]. The

---

[1] This is equivalent to Eq. (29) in Ref. [10]. However, the unknown parameters in Ref. [10] are the $||E_i||$ values, equal to $F_i + v\, A_i / B_i$, where A_i values are defined thereafter. In addition, Eq. (29) in Ref. [10] can be further simplified considering both Eq. (5) and that U_{ij} are components of the eigenvectors of the diffusion matrix $\mathbf{D}$.

latter hypothesis leads to a diagonal matrix, $\mathbf{K}$, defined by $K_{ii} = k_i$ with $(1 \leq i \leq N-1)$ and a zero value elsewhere. In the present application, a full partition matrix is considered, allowing the off-diagonal terms of $\mathbf{K}$ to contribute to the dendrite growth kinetics.

Eq. (7) could also be compared to usual expressions proposed in the literature when matrices $\mathbf{K}$ and $\mathbf{D}$ are diagonal. This reduces the $\mathbf{A}$ vector to the $\mathbf{\Delta w}$ vector, which yields simplified expressions for the F_i coefficients:

$$F_i = -v \, \frac{w_i^{ls} - w_i^{sl}}{D_i} \, \frac{\zeta_i}{\zeta_i - 2\, k_i} = G_{\chi_i} \, \xi_{\chi_i} \quad \forall\, i \; (1 \leq i \leq N-1) \tag{11}$$

This later expression is similar to the one proposed by Kurz *et al.* [1, 20] (see p.234-235 and Eq. A7.22c in [1]) for a binary alloy, where G_{χ_i} and ξ_{χ_i} are respectively the solute gradient in the liquid at the solid-liquid interface and the correction factor induced by the growth velocity, both for component i.

- *Temperature at dendrite tip*

The previous expressions provide relations determining the (r, v) couple at the dendrite tip (or the Péclet numbers) for a given set of interface compositions. However, these relations have to be coupled with the temperature at the dendrite tip, T, also considering the Gibbs-Thomson effect associated to the selected tie line of the phase diagram. In the present approach, the dendrite tip temperature is function of the set of interface compositions, $\mathbf{w}^{ls}$, and the excess Gibbs free energy in the solid phase, ΔG_κ^s, created by the tip curvature, κ:

$$T = \mathrm{F_L}\left(\mathbf{w}^{ls}, \Delta G_\kappa^s\right) \tag{12}$$

Similarly, the composition in the solid phase, $\mathbf{w}^{sl}$, i.e. at the dendrite tip, is also a function of the liquid composition, $\mathbf{w}^{ls}$, considering the selected tie line:

$$\mathbf{w}^{sl} = \mathrm{F_{W^S}}\left(\mathbf{w}^{ls}, \Delta G_\kappa^s\right) \tag{13}$$

The total undercooling at the dendrite tip, ΔT, is expressed as the sum of the curvature undercooling, ΔT_κ, and the chemical undercooling, ΔT_χ:

$$\Delta T = T_L - T = \Delta T_\kappa + \Delta T_\chi \tag{14a}$$

$$\Delta T_\kappa = T_L^{ls} - T \tag{14b}$$

$$\Delta T_\chi = T_L - T_L^{ls} \tag{14c}$$

where T_L is the liquidus temperature at the nominal (far-field) composition, $\mathbf{w}^0$, and T_L^{ls} is the liquidus temperature at the interface composition, $\mathbf{w}^{ls}$, without consideration of the curvature, $T_L = \mathrm{F_L}\left(\mathbf{w}^0, \Delta G_\kappa^s = 0\right)$ and $T_L^{ls} = \mathrm{F_L}\left(\mathbf{w}^{ls}, \Delta G_\kappa^s = 0\right)$. The excess Gibbs free energy associated to the curved solid phase, ΔG_κ^s, is directly proportional to the curvature at the parabolic dendrite tip, κ, the energy of the solid-liquid interface, γ, assumed constant and isotropic, and the molar volume of the solid phase, V_M^s, that varies with temperature and composition, $\mathrm{F_{V_M}}$:

$$\Delta G_\kappa^s = \kappa \, \gamma \, V_M^s \tag{15}$$

$$V_M^s = \mathrm{F}_{\mathrm{V_M}} \left(\mathbf{w}^{sl}, T \right) \tag{16}$$

$$\kappa = \frac{2}{r} \tag{17}$$

The effect of curvature is only considered to modify the Gibbs free energy of the solid phase, i.e. not that of the liquid phase. However, note that modifying the Gibbs free energy of the solid phase by ΔG_κ^s will change the equilibrium common tangent and modify both compositions $\mathbf{w}^{sl}$ and $\mathbf{w}^{ls}$. The above treatment of curvature on thermodynamic equilibrium is a more general form of the usual linearization that approximates the curvature undercooling by the expression $\Delta T_\kappa = \Gamma \, \kappa$, where Γ is the Gibbs-Thomson coefficient. Also, note that setting $\Delta G_\kappa^s = 0$ in equations (12) and (13) simply corresponds to a solid-liquid interface with zero curvature, i.e., a planar front.

- *Constitutional supercooling criterion*

The extension of the constitutional supercooling criterion [5] to multicomponent alloys was first proposed by Bobadilla *et al.* [9] and generalized to consider cross-diffusion of solute species in the liquid [10]. By analogy with the previously introduced stability analysis, the critical velocity, v_c, is the solution of Eq. (5) when the curvature contribution $\Gamma\omega^2$ is dropped. Because v_c is typically $\sim 10^{-7} - 10^{-6}$ m s^{-1}, the ζ_i parameters in Eq. (8) can be approximated as $-2\omega B_i / v_c$. As this ζ_i value is large in magnitude, the solution of Eq. (7) is $F_j = -v_c A_j / B_j$. The components of the $\mathbf{A}$ vector are then expressed using Eq. (9) in the limiting conditions of instability on a planar growth front in steady state, i.e., when $\mathbf{\Delta w}$ reduces to $(\mathbf{w}^{ls} - \mathbf{w}^{sl}) = w_i^0 \, (1/k_i - 1)_{1 \le i \le N-1}$. In a coupled thermodynamic resolution approach, k_i coefficients should also be estimated at the solidus temperature, $T_S = \mathrm{F_S}\left(\mathbf{w}^0, \Delta G_\kappa^s = 0\right)$, without curvature effects, as expected for a planar front. Introduction of these considerations to evaluate the A_j coefficients yields, for any j index:

$$F_j = -\frac{v_c}{B_j} \sum_{k=1}^{N-1} U_{jk}^{-1} w_k^0 \left(\frac{1}{k_k} - 1 \right) \tag{18}$$

Combining Eqs (5) and (18) yields an expression for the critical velocity:

$$v_c = -\frac{G}{\displaystyle\sum_{i=1}^{N-1} m_i \sum_{j=1}^{N-1} \left[\frac{U_{ij}}{B_j} \sum_{k=1}^{N-1} U_{jk}^{-1} w_k^0 \left(\frac{1}{k_k} - 1 \right) \right]} \tag{19}$$

- *Absolute stability criterion*

The condition for interface stabilisation at high growth velocity can be similarly investigated. We seek a solution of Eq. (5) for high wavelengths (small wavenumber ω) and high velocities, i.e., high v/ω ratio (equivalent to high Péclet number) for any i solute species. Considering that the so-called velocity at absolute stability, v_a, increases but remains finite while the perturbation wavelength tends to infinity (or wavenumber ω tends toward zero), the ζ_i parameters in Eq. (7) can be approximated by the ratio $2\left(\omega B_j/v_a\right)^2$ considering Eq. (8). Additionally, the ratio ω/v_a is small and decreases toward zero, so the first term on the left-hand-side of Eq. (7) can be dropped, reducing Eq. (7) to:

$$\sum_{i=1}^{N-1} K_{ki} \left[\sum_{j=1}^{N-1} U_{ij} F_j\right] = -\frac{\omega^2}{v_a} \sum_{j=1}^{N-1} U_{kj}\, A_j\, B_j \tag{20}$$

With the definition of coefficients $\widetilde{\mathbf{X}} = \widetilde{X_i}$ $(1 \leq i \leq N-1)$ as:

$$\widetilde{X_i} = \frac{v_a}{\omega^2} \sum_{j=1}^{N-1} U_{ij} F_j \tag{21}$$

Eq. (20) can be solved for v_a by considering the $\widetilde{X_i}$ coefficients as the new unknown parameters. Evaluating the A_i components in Eq. (20) as in Eq. (18) allows the $\widetilde{X_i}$ coefficients to be expressed for any index as:

$$\widetilde{X_i} = -\sum_{j=1}^{N-1}\sum_{k=1}^{N-1}\sum_{l=1}^{N-1} K^{-1}_{ik} w^0_l \left(\frac{1}{k_l} - 1\right) U_{kj}\, U^{-1}_{jl}\, B_j \tag{22}$$

where $\mathbf{K^{-1}}$ is the inverse matrix of the $\mathbf{K}$ matrix. The $\widetilde{X_i}$ coefficients can now be introduced to Eq. (5) in the limit of small wave number to estimate the absolute velocity, v_a. Additionally, because $\Gamma\omega^2 \gg G$ at high growth velocities, the temperature gradient can be neglected. This yields the expression for the velocity of absolute stability:

$$v_a = \frac{1}{\Gamma} \sum_{i=1}^{N-1} m_i \left(\frac{v_a}{\omega^2} \sum_{j=1}^{N-1} U_{ij} F_j\right) = \frac{1}{\Gamma} \sum_{i=1}^{N-1} m_i \widetilde{X_i} \tag{23}$$

2.2. Resolution and implementation

The resolution algorithm is summarized in Fig. 2. It aims to find the curvature radius at the dendrite tip, r, and its corresponding interface compositions, $\mathbf{w}^{sl}$ and $\mathbf{w}^{ls}$, temperature, T, and undercoolings, ΔT, ΔT_χ and ΔT_κ, for a given alloy composition, $\mathbf{w}^0$, temperature gradient, G, and growth velocity, v. To find possible solutions to the set of equations, we develop a scan over a large interval of growth velocities, $[v_{min}, v_{max}]$ where $v_{min} < v_c$ and $v_{max} > v_a$, as solutions may only exist for velocities at which the planar growth front is unstable, i.e., $v_c < v < v_a$.

The interfacial energy, γ, and the selection constant, σ, are given. The diffusion matrix in the liquid phase is fixed and evaluated at the nominal composition of the alloy and its liquidus temperature, $\mathbf{D} = \mathbf{D}\left(\mathbf{w}^0, T_L\right)$, and its eigenvalues $\mathbf{B}$ and eigenvectors $\mathbf{U_{\cdot,j}}$ are subsequently computed. We begin an iterative loop with initialized values of the curvature radius, $r^{(0)} \simeq 1 \times 10^{-8}\,\mathrm{m}$ (i.e., assuming a very small value), the interface temperature, $T^{(0)} = T_L$, and compositions chosen at the equilibrium liquidus temperature of the alloy, $\mathbf{w}^{sl(0)} = \mathrm{F}_{\mathrm{W^S}}(\mathbf{w}^0, \Delta G^s_{\kappa=0})$ and $\mathbf{w}^{ls(0)} = \mathbf{w}^0$.

Every iteration, numbered n $(n \geq 1)$, begins with a calculation of the thermodynamic equilibrium between the solid and liquid phases in the presence of a curved interface. This is performed by computing the molar volume of the solid phase, $V_M^{s(n)}$, at the current temperature, $T^{(n-1)}$, and composition, $\mathbf{w}^{sl(n-1)}$, while considering the excess Gibbs free energy, $\Delta G_\kappa^{s(n)}$, due to the curvature of the tip with radius $r^{(n-1)}$. Thermodynamic equilibrium using the modified Gibbs free energy for the solid phase gives new solid compositions, $\mathbf{w}^{sl(n)}$, that can be input in the extension of the Ivantsov solution [10] to compute a liquid composition, $\mathbf{w}^{ls(n)}$, leading to a new equilibrium temperature of the interface, $T^{(n)}$, which modifies the values of the undercoolings, $\Delta T^{(n)}$, $\Delta T_\chi^{(n)}$ and $\Delta T_\kappa^{(n)}$. The curvature undercooling and the actual curvature allow the Gibbs-Thomson coefficient, $\Gamma^{(n)}$, to be estimated from Eq. (24):

$$\Gamma = \frac{\Delta T_\kappa}{\kappa} \tag{24}$$

The last steps are to compute the $\mathbf{K}^{(n)}$ matrix, $\mathbf{A}^{(n)}$ vector, and the $\mathbf{F}^{(n)}$ matrix in order to apply the marginal stability criterion and update the tip radius, $r^{(n)}$. Upon convergence with criterion $\left| r^{(n)}/r^{(n-1)} - 1 \right| < \varepsilon$ where ε is of the order of 10^{-6}, relevant estimation of all fields is reached. It was checked that the absence of convergence was linked to a velocity close to the bounds of the $[v_c,\, v_a]$ interval. In order to draw a dendrite tip kinetics as a function of the velocity, as mentioned previously, the algorithm reported in Fig. 2 is scanned over the interval of velocity $[v_{min},\, v_{max}]$ with a velocity step based on a geometrical progression. It is also worth noticing that several quantities, namely ΔT_χ and ΔT_κ, are only computed for interpretation and illustration of the results. The value of the Γ coefficient at the maximum velocity for which convergence was reached, i.e., close to v_a, was solely used in Eq. (23) to compute the absolute velocity. This explains the presence of the last step of the algorithm in Fig. 2.

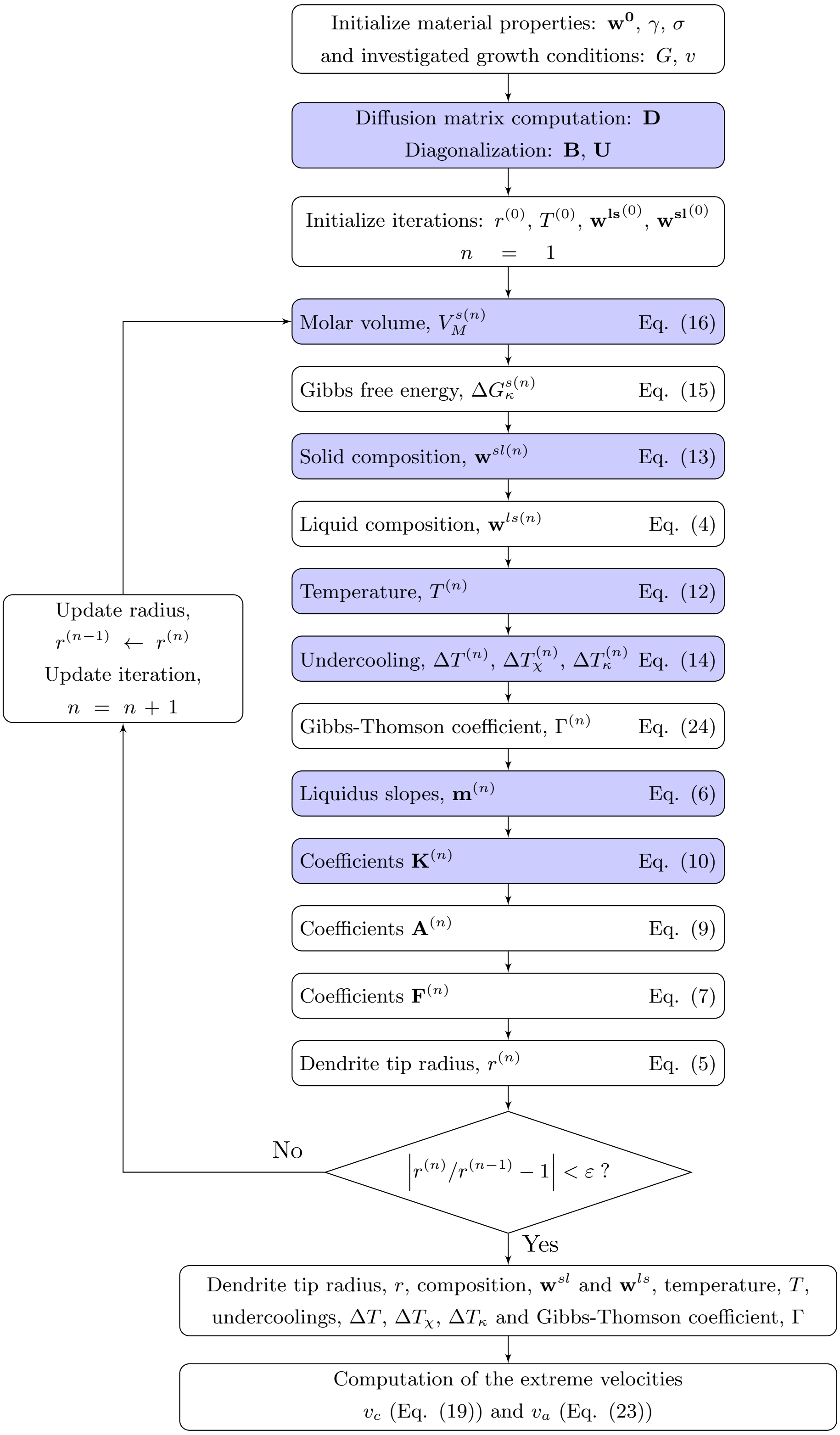

Figure 2: Algorithm describing the successive steps to estimate the dendrite tip interface features for a given growth velocity, v, of an alloy with composition $\mathbf{w}^0$. Blue-coloured boxes indicate direct access to thermodynamic calculations [35].

3. Application to IN718

The application presented hereafter focusses on the IN718 nickel-base superalloy. The widespread use of this alloy in diverse solidification processes justifies the choice. One can cite casting [36], welding [37, 38], laser cladding [39] and additive manufacturing [40, 41], also covering a large range of cooling conditions, including both solidification velocity and temperature gradient [42]. Such observations support the interest in investigating the relations between solidification features at the dendrite tip and the growth velocity while considering coupling with thermodynamic databases. Comparisons with uncoupled strategies is the topic of Section 4, which will include the effects of linearizing the phase diagram and of using a Gibbs-Thomson coefficient coming from literature, as well as simplifying the diffusion matrix to its diagonal terms. Hence, the present calculation for IN718 can be seen as the reference solution for these upcoming approximations. The composition of the eight components used in this study is provided in Tab. 1, and is taken from a study of selective laser melting, a powder-bed-fusion additive manufacturing technique [40].

As previously stated, the diffusion matrix in the liquid phase is computed at the liquidus temperature of the alloy and at the alloy composition by calling thermodynamic databases. For this purpose, it is worth noting that the database TCNI10 [43] computes the chemical potentials of the solute components in the liquid phase and their partial derivatives with respect to compositions, while the MOBNI5 database [44] gives access to mobility of the solute components in the liquid phase, which are all functions of composition and temperature. The methodology for computing the diffusion coefficients is described elsewhere [45]. The full diffusion matrix is reported in Appendix A with the associated eigenvalues and the transfer matrix corresponding to the set of unit eigenvectors.

The properties of the IN718 alloy are summarized in Tab. 2. The selection parameter, σ, has been fixed to a value close to $(2\pi)^{-2}$. Liquidus and solidus temperatures at the nominal composition are also indicated [43]. In the conditions investigated hereafter, the temperature gradient, $G = 10\,000\,\mathrm{K\,m^{-1}}$, is imposed so the dendrite tip velocity is the independent variable. Under steady cooling conditions, the tip velocity is equivalent to the velocity of the isotherms, $|\dot{T}|/G$, where $\dot{T}$ is the solidification cooling rate.

The range of values reported in literature for the solid-liquid interface energy of IN718 is large, which is likely due to the lack of definite and clear measurements serving as reference. Studies provide theoretical estimations for pure nickel from $0.18\,\mathrm{J\,m^{-2}}$ [46] to $0.382\,\mathrm{J\,m^{-2}}$ [47]. Similarly, results based on molecular dynamics simulations vary, with $0.197\,\mathrm{J\,m^{-2}}$ [48], $0.256\,\mathrm{J\,m^{-2}}$ [49] and $0.31\,\mathrm{J\,m^{-2}}$ [50]. Other estimations for pure nickel rely on experiments. This is the case with the value $0.3\,\mathrm{J\,m^{-2}}$ proposed by Kelton [51] or indirect measurements using nanoparticles by Wu *et al.* [52] giving $0.332\,\mathrm{J\,m^{-2}}$. Hereafter, we use the value $0.37\,\mathrm{J\,m^{-2}}$ from the estimation by Wheeler *et al.* [53], which used a formula originally proposed by Coriell and Turnbull [54], as it is commonly encountered in literature [55, 56, 57].

Fig. 3 presents (a) the dendrite tip radius as a function of the growth velocity and (b) the corre-

Chemical elements	Cr	Fe	Nb	Mo	Ti	Al	C	Ni
Nominal composition, w^0 [wt.%]	18.2	18.9	5.1	3.1	0.9	0.29	0.025	Balance

Table 1: Mass composition of the IN718 nickel-base superalloy [40].

Property	Symbol	Value	Unit	Ref	Fig.
Interfacial energy	γ	0.37	[J m^{-2}]	[54, 53]	3-6
Liquidus temperature	T_L	1613.34	[K]	[43]	3-6
Solidus temperature	T_S	1520.26	[K]	[43]	3-6
Selection parameter	σ	0.02533	[-]	[20]	3-12
Gibbs-Thomson coefficient					
Pure Ni	Γ_{Ni}	$1.91 \cdot 10^{-7}$	[K m]	[49]	10
IN718 (Computed)	Γ	$3.355 \cdot 10^{-7}$	[K m]	-	4 (b), 7-9, 11-12
Temperature gradient	G	10 000	[K m^{-1}]	-	3-12

Table 2: Physical properties and simulation parameters for the computation of the dendrite growth kinetics of the IN718 nickel-base superalloy.

sponding interface temperature (T). At a given velocity, the difference between the liquidus temperature of the alloy, T_L, and the equilibrium temperature without curvature, T_L^{ls}, is simply the chemical undercooling (Eq. 14c), and the difference between T_L^{ls} and T is the curvature undercooling (Eq. 14b). Both contributions are shown by also drawing the curve T_L^{ls}. The limiting values defining the range of non-planar growth, $[v_c, v_a]$, are marked with vertical lines. The lowest velocity for dendritic growth at which a solution of the system of equations is found appears at a slightly higher velocity, $\simeq 8 \times 10^{-7}$ m s^{-1}, than the constitutional supercooling criterion, $v_c = 3.441 \times 10^{-7}$ m s^{-1}. This is due to the paraboloidal shape of the dendrite, as the constitutional supercooling criterion assumes a planar front. One can notice that the lowest possible velocity value for the dendrite tip coincides with a large tip radius on the order of 100 µm and negligible curvature undercooling, as expected when approaching the planar-front limit. Consequently, the value of v_c is associated with the operating point of the planar front at the solidus temperature, T_S. By increasing the velocity, the tip radius progressively decreases and the classical power law, $r \propto v^{-1/2}$, is observed as the tip temperature continuously decreases from approximately the liquidus temperature, $T_L = 1613.34$ K, to the solidus temperature, $T_S = 1520.26$ K. At high growth rates, i.e., when approaching the absolute stability limit, $v_a = 4.379$ m s^{-1}, the interface is stabilized, and an increasing tip radius and vanishing curvature undercooling is again observed. To compute v_a from Eq. (23), the partition matrix, $\mathbf{K}$, is computed at the solidus temperature, and is reported in Appendix A. It is worth noting that the curvature undercooling, ΔT_κ, is zero for planar-front conditions, but reaches a maximum $\simeq 14.2$ K at velocity $\simeq 1.12$ m s^{-1}.

For several decades, microstructural models have been developed using an empirical $v(\Delta T)$ relationship to compute the dendrite tip velocity [58, 59, 60, 61], despite progress in the understanding of dendrite growth kinetics. This provides a convenient way to link the local temperature predicted from a heat flow model to the local growth velocity of the dendrite. Vice-versa, knowing the isotherm velocities and assuming steady heat flow permits estimation of the leading dendrite tip undercooling located at the growth front. For such purposes, a simple $v(\Delta T)$ relationship is more efficient than solving the set of equations presented in Section 3. Fig. 4 (a) presents the dendrite tip velocity as a function of the total undercooling and the contribution due to curvature. A continuous increase of the velocity with the total undercooling is found, while the maximum of the curvature undercooling is retrieved at $v \approx 1.12\,\mathrm{m\ s^{-1}}$. A fit is proposed considering a power law evolution for the growth velocity as a function of the total undercooling ($v = 1.09 \cdot 10^{-10} \Delta T^{5.23}$). Due to its simple form, a perfect fit is not obtained, but this could be improved using a polynomial form, as commonly proposed in literature [61], or a smaller range of undercoolings over a smaller range of velocities [62, 63]. The evolution of the curvature undercooling, ΔT_κ, with curvature, κ, is also shown in Fig. 4 (b) for the entire undercooling range. A perfect linear evolution is observed between both variables, and the value $\Gamma = 3.355 \times 10^{-7}\,\mathrm{K\ m}$ reported in Tab. 2 is calculated from Eq. (24). The linear behavior of this curve justifies the approximation of a constant Gibbs-Thomson effect, despite the clear limitations of this approach, as discussed by Jácome *et al.* [64]. Ferreira also demonstrates composition effects on the estimation of the Gibbs-Thomson coefficient [65] based on CALPHAD computations developed on multicomponent alloys. The use of relevant databases in such estimations was also highlighted. Consequently, further coupling of the algorithm may be performed with additional databases that would provide adequate estimation of the interfacial energy with temperature and composition. In such situations, the curvature undercooling might no longer be well-estimated by a linear relationship with the curvature, and the Gibbs-Thomson coefficient would no longer be well-approximated by a constant value.

The evolution of the segregation coefficients, $k_i = w_i^{sl}/w_i^{ls}$, and liquidus slopes, $m_i = \partial T / \partial w_i^{ls}\big|_{w_j^{ls}, j \neq i}$ are drawn for all i-solute species in Figures 5 (a) and (b) over the same range of velocity. Large variations are found when increasing the velocity for both the segregation coefficient of aluminum and the liquidus slopes of aluminium and carbon. Smaller variations take place for titanium and niobium, but this does not mean that they can be neglected. It is important to remember that the current implementation of the thermodynamic coupling with CALPHAD calculations assumes that the solid-liquid interface is always at thermodynamic equilibrium. Hence, the reported evolution of the k_i and m_i values with velocity does not reflect the results of kinetic effects such as solute trapping [21, 66] or solute drag [67, 68], but only the effects of temperature and diffusion kinetics on the selected tie line for a multicomponent alloy. Thus, it may be incorrect to attribute an observed increase in partition coefficient with velocity entirely to kinetic effects, as thermodynamic effects can also contribute when considering the full phase diagram. Interestingly, this is also observed when considering the on-diagonal coefficients of the partition matrix, K_{ii}, even though Eq. (10) indicates that the K_{ii} coefficients are generally not equal to the partition coefficients, k_i. As an example, in the present case, it is observed that $k_{Al} \approx 0.987$ when $T \approx T_L$ and $k_{Al} \approx 1.599$ when $T \approx T_S$, at the low and high velocity limits, respectively (Fig. 5 (a)). For the same temperatures, the values of the $\mathbf{K}$ matrices reported in Appendix A are $K_{Al-Al}(T_L) = 0.95981$ and $K_{Al-Al}(T_S) = 1.57365$. Hence, $K_{Al-Al} \approx k_{Al}$, indicating that the IN718 phase diagram may be well-approximated by a multi-linear phase diagram at this temperature. These observations and the evolution of the $\mathbf{K}$ matrix foreshadow possible limitations encountered when assuming constant values of these coefficients to compute dendrite growth velocity for multicomponent non-dilute alloys, which is a typical practice reported in literature.

Finally, the composition profiles in the liquid phase for $v = 0.3\,\mathrm{m\ s^{-1}}$ are shown in Fig. 6. For each alloying element, the ratio of the local composition to its interface composition, $w(\eta)/w^{ls}$ or $w(z/r)/w^{ls}$, is drawn as a function of the position in the liquid, $\eta \geq 1$ or $z/r \geq 1/2$. Both positive and negative

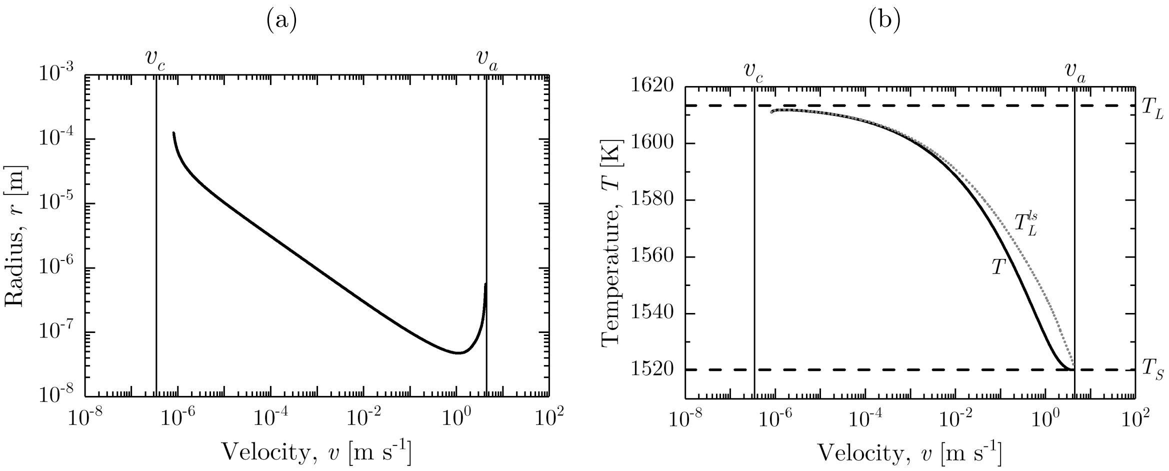

Figure 3: Dendrite growth kinetics with (a) tip radius, r, versus velocity, v, and (b) tip temperature versus velocity (plain line, T) with and (dotted line, T_L^{ls}) without curvature undercooling at the solid-liquid interface. The range of dendritic growth, $[v_c, v_a]$, and the solidification range of the alloy, $[T_S, T_L]$, are added.

segregation in the liquid, i.e. accumulation and depletion ahead of the interface, are observed, corresponding to segregation coefficients lower than and higher than unity, respectively, as reported in Fig. 5 (a). Non-monotonic evolution of several elements is revealed — while this is most obvious for aluminum, the diffusion fluxes of all solute components are indeed modified by the off-diagonal terms in the diffusion matrix, so their composition gradients differ from those obtained by only considering the on-diagonal diffusion coefficients.

It is also worth mentioning that some physical properties are poorly known, in particular those linked to the solid-liquid interface. We have reported estimations for the interfacial energy and chosen to use the value $\gamma = 0.37\,\mathrm{J\,m^{-2}}$. With no clear estimation for the selection parameter for the IN718 nickel-base superalloy, we have used $\sigma = \sigma^* = (2\pi)^{-2}$. Measurements for model alloys report values for σ that are lower by around 20 % compared to σ^* [69, 70]. Two additional simulations were performed by decreasing σ and γ by 20 % from their values given in Tab. 2. In a range of small undercooling, the expected deviations from the reference solution are found with very similar intensities. For instance, with a 10 K total undercooling, the velocity decreases to $0.479\,\mathrm{mm\,s^{-1}}$ when decreasing the selection parameter by 20 % and increases to $0.692\,\mathrm{mm\,s^{-1}}$ when decreasing the interfacial energy by 20 %, to be compared with the value $0.575\,\mathrm{mm\,s^{-1}}$ read on the plain line in Fig. 4 (a) when applying a magnification. However, at large undercooling, the selection parameter has little effect so that the curve is almost superimposed to the total undercooling displayed in Fig. 4 (a) while the interfacial energy still significantly influences the growth velocity.

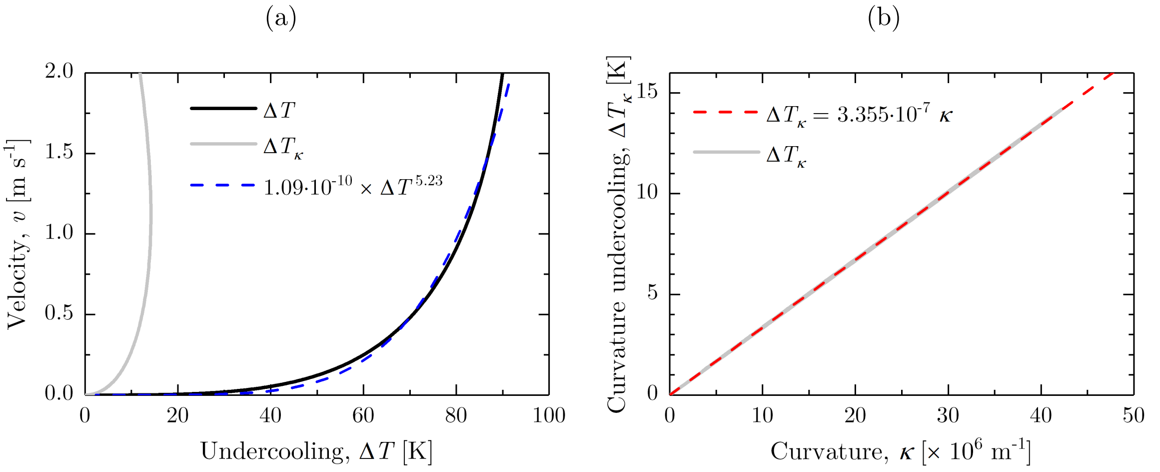

Figure 4: Dendrite growth kinetics with (a) (plain line) total tip undercooling, ΔT, and (grey line) curvature undercooling, ΔT_κ, versus growth velocity, v and (b) curvature undercooling, ΔT_κ, versus curvature, κ. Dashed curves are proposed interpolations for (blue) tip velocity, v, and (red) curvature undercooling, ΔT_κ.

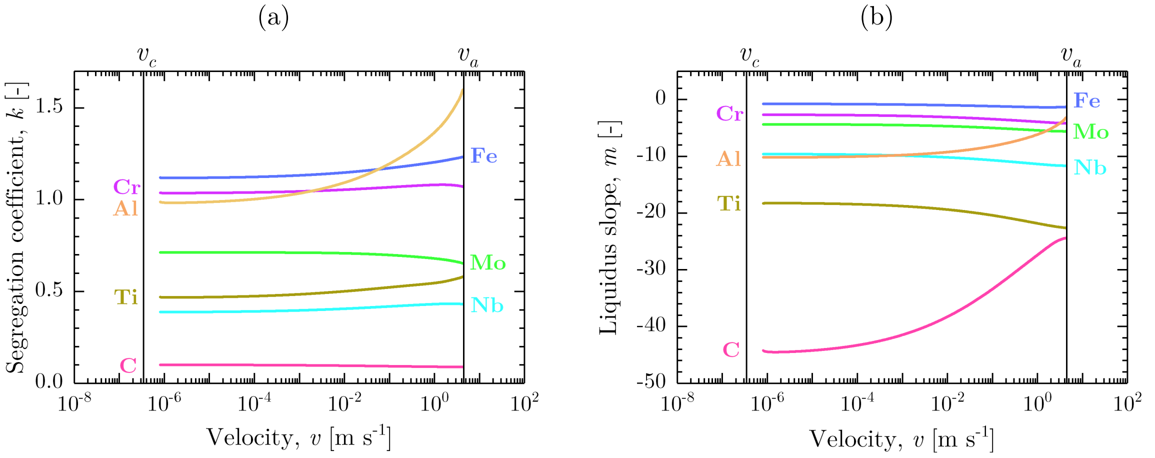

Figure 5: Computed (a) segregation coefficient, k_i, and (b) liquidus slope, m_i, with tip velocity, v, for all seven i-solute components of alloy IN718 (Tab. 1).

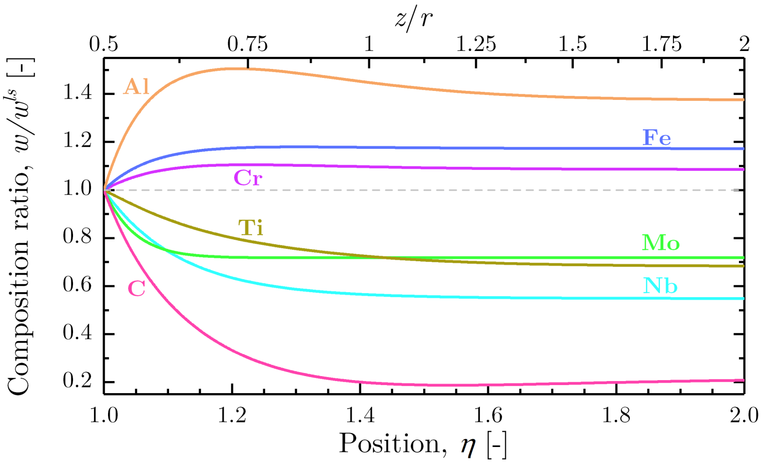

Figure 6: Ratio between local and interface compositions, ($w(\eta)/w^{ls}$ or $w(z/r)/w^{ls}$) of the alloying elements (Tab. 1) for $v = 0.3\,\mathrm{m\,s^{-1}}$. Evolution are reported versus the η paraboloidal coordinate. Coordinate $\eta = 1$ corresponds to the solid-liquid interface at the dendrite tip (also $z = r/2$) and $\eta = 2$ is located at a distance equal to $3/2\,r$ ($z = 2\,r$) (Fig. 1).

4. Discussion

The previous section and its results serve as a reference solution for the improved dendrite tip kinetics, which consider: $i-$ a full diffusion matrix, $\mathbf{D}(T_L, \mathbf{w}^0) = (D_{ij}(T_L, \mathbf{w}^0))_{1\le(i,j)\le N-1}$ as given in Appendix A; $ii-$ coupling with CALPHAD-computed interface equilibrium between the solid and liquid phases, i.e., evaluating the liquidus slopes, $m_i(T, \mathbf{w}^{ls})$ $(1 \le i \le N-1)$, and partition coefficients, $K_{ij}(T, \mathbf{w}^{ls})$ $(1 \le (i,j) \le N-1)$, at each tip temperature, T, and interface composition, $\mathbf{w}^{ls}$; and $iii-$ an updated estimation of the Gibbs-Thomson coefficient, Γ. In the present section, we discuss the effects of common approximations in the literature, attempting to isolate them individually although they are typically combined. The six cases considered and their approximations are summarized in Tab. 3. The first four cases concentrate on approximating thermodynamic properties by using constant segregation coefficients, k, liquidus slopes, m, and a Gibbs-Thomson coefficient, Γ. This last parameter is fixed to the value previously estimated in Fig. 4 (b) for the *Reference* case (Tab. 2). In practice, this means that the steps associated to thermodynamic calculations, highlighted in blue in Fig. 2, are ignored. Also, because the Gibbs-Thomson coefficient is predetermined, the molar volume and the interface energy are no longer needed. The fifth and sixth cases in Tab. 3 evaluate the effect of using a diagonal matrix and departing from interface equilibrium [21, 66], respectively. Tab. 4 summarizes the computed values for the constitutional supercooling velocity and absolute velocity for all the cases in Tab. 3. Each case will be successively compared with the reference curves presented in Section 3, which are marked with dashed gray lines in the forthcoming Figs. 7–12. Before beginning the comparisons, it is worth noting that the usual uncoupled strategy with CALPHAD equilibrium calculations was applied to several solutions found in literature. These include alloys as Ag-Cu [20], Al-Cu [71], Al-Si-Mg [72], IN718 [28] or even succinonitrile-acetone system [62, 63], also considering the effect of departing from interface equilibrium. The ternary system studied by Hunziker [10] was also investigated with similar approach. Using the

Case	*Reference*	*Multi-linear*	*Multi-binary*	*Pseudo-binary*	*Curvature*	*Diagonal diffusion*	*Non-equilibrium*
Diffusion	$D_{ij}(T_L, \mathbf{w}^0)$	*Ref.*	*Ref.*	$\overline{D}$	*Ref.*	$D_{ii}(T_L, \mathbf{w}^0)$	*Ref.*
Partition	$\mathbf{K}(T)$	$k_i(T_L, \mathbf{w}^0)$	$k_i^{bin}(T_L^{bin}(w_i^0))$	$\overline{k}$	$k_i(T_L, \mathbf{w}^0)$	$k_i(T_L, \mathbf{w}^0)$	$k_i(T_L, \mathbf{w}^0, v)$
Slope	$\mathbf{m}(T, \mathbf{w}^{ls})$	$m_i(T_L, \mathbf{w}^0)$	$m_i^{bin}(T_L^{bin}(w_i^0))$	$\overline{m}$	$m_i(T_L, \mathbf{w}^0)$	$m_i(T_L, \mathbf{w}^0)$	$m_i(T_L, \mathbf{w}^0, v)$
Curvature	$\gamma, V_M^s(\mathbf{w}^{\mathbf{sl}}, T)$	Γ	Γ	Γ	Γ_{Ni}	Γ	Γ
Tables		5	6	7		5	5, 8
Figures	3-6	7	8	9	10	11	12

Table 3: Approximation cases for comparison with the reference solution corresponding to the simulation of Section 3 for the growth kinetics of the IN718 Ni-base superalloy. The matrix $\mathbf{D}(T_L, \mathbf{w}^0) = (D_{ij}(T_L, \mathbf{w}^0))_{1 \leq (i,j) \leq N-1}$ is given in the Appendix A and the coefficients $k_i(T_L, \mathbf{w}^0)$ and $m_i(T, \mathbf{w}^0))$ $(1 \leq i \leq N-1)$ are provided in Tab. 5 [43].

Case	v_c [m s^{-1}]	v_a [m s^{-1}]	Figs
Reference	3.441×10^{-7}	4.379	3
Multi-linear	3.441×10^{-7}	3.751	7
Multi-binary	1.624×10^{-6}	0.653	8
Pseudo-binary	5.587×10^{-7}	0.721	9
Curvature	3.441×10^{-7}	6.601	10
Diagonal diffusion	3.077×10^{-7}	5.264	11
Non-equilibrium	3.441×10^{-7}	0.678	12

Table 4: Values of constitutional supercooling velocity, v_c (Eq. 19), and absolute stability velocity, v_a (Eq. 23), for all cases (Tab. 3). The latter is computed considering that $K_{ik}^{-1} = 0\,(i \neq k)$ and $K_{ii}^{-1} = 1/k_i$ (Eq. 22) except in the *Reference* case where inversion of the partition matrix $\mathbf{K}$ (Appendix A) provides estimation of the K_{ik}^{-1} coefficients.

material data provided in references [20, 10, 62, 63], perfect matches were found when comparing the $v(T)$ and $r(v)$ curves, validating the following comparisons and discussions.

4.1. Multi-linear phase diagram

The *Multi-linear* approximation is based on using constant segregation coefficients, $k_i(T_L, \mathbf{w}^0)$, and liquidus slopes, $m_i(T_L, \mathbf{w}^0)$ $(1 \leq i \leq N-1)$, all computed at the liquidus temperature of the alloy, $T_L(\mathbf{w}^0)$, and at the alloy composition, $\mathbf{w}^0$. Because these phase diagram properties are assumed constant, this set of approximations is often referred to as a “linearized phase diagram”. This strategy is commonly reported in literature [9, 73]. Tab. 5 presents the properties of the linearized phase diagram calculated using the TCNI10 database [43]. Note that the values coincide with those reported at low velocity in Figs. 5 (a) and (b), i.e., for a tip temperature very close to the liquidus temperature. The full diffusion matrix, as reported in Appendix A, is applied in the liquid phase. As no thermodynamic coupling is considered, the previously reported estimation of the Gibbs-Thomson coefficient, $\Gamma = 3.355 \times 10^{-7}$ K m, is used to estimate the curvature undercooling (Eq. 24, Fig. 4 (b), Tab. 2).

Evolution of the dendrite tip radius and the growth undercooling as a function of velocity are reported in Fig. 7 as solid black curves. In Fig. 7, no difference is observed from the *Reference* case within the

Solute component	Cr	Fe	Nb	Mo	Ti	Al	C
Liquidus slope, $m_i(T_L, \mathbf{w}^0)$ [K wt.%$^{-1}$]	-2.646	-0.737	-9.567	-4.339	-18.17	-10.254	-44.98
Segregation coefficient, $k_i(T_L, \mathbf{w}^0)$ [wt.% wt.%$^{-1}$]	1.035	1.117	0.387	0.712	0.465	0.975	0.101

Table 5: Liquidus slopes, $m_i(T_L, \mathbf{w}^0)$, and segregation coefficients, $k_i(T_L, \mathbf{w}^0)$ ($1 \leq i \leq N-1$), computed at the composition, $\mathbf{w}^0$, and liquidus temperature, $T_L(\mathbf{w}^0)$, of the IN718 Ni-base superalloy (Tab. 1) for case *Multi-linear* (Tab. 3) [43].

.

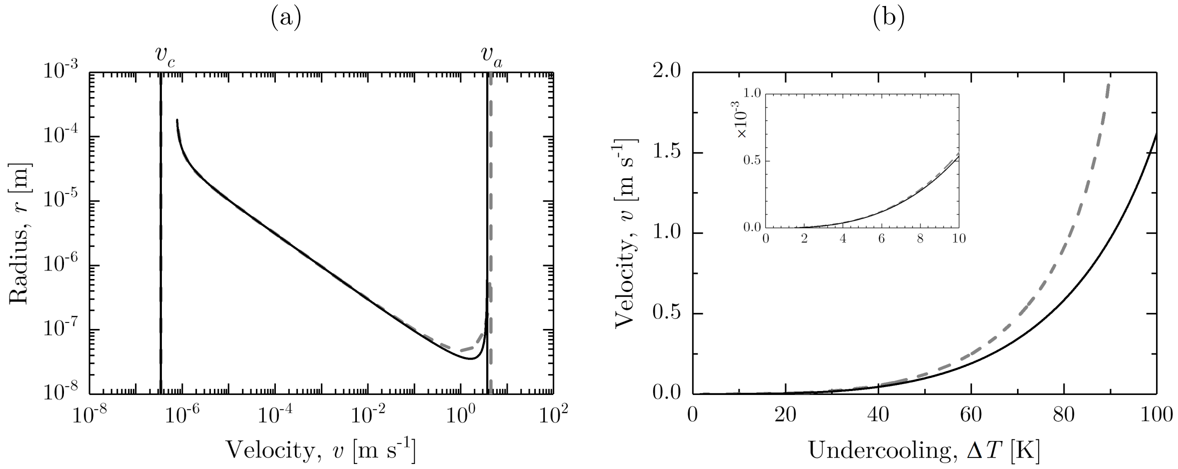

Figure 7: Dendrite tip kinetics comparing (thin plain lines) case *Multi-linear* (Tables 3 and 5) with (thick dashed gray lines) the *Reference* case to highlight the role of thermodynamic coupling when simplifying the phase diagram properties. Comparisons include (a) the tip radius versus velocity and (b) the undercooling versus velocity.

velocity range $[v_c, 10^{-1}]$ m s^{-1}. At higher velocities, the *Multi-linear* approximation predicts smaller radii and larger undercoolings. The main reason for these differences is explained by contrasting the variations of the liquidus slopes and segregation coefficients with velocity, as shown in Fig. 5, with the constant values reported in Tab. 5. One might conclude that the *Multi-linear* approximation is relevant for applications at low velocities, e.g., for conventional casting, but not for rapid solidification processes like additive manufacturing, which can reach velocities higher than 1 m s^{-1}. Additionally, Tab. 4 shows no difference between the v_c values of the *Multi-linear* and *Reference* cases. This is expected, as Eq. (19) is applied when $k_i(T_L, \mathbf{w}^0)$ and $m_i(T_L, \mathbf{w}^0)$ ($1 \leq i \leq N-1$) are evaluated close to the liquidus temperature in both cases. However, the value of v_a changes between the two cases, as the *Multi-Linear* approximation still uses the constant k_i coefficients evaluated near the liquidus temperature, while the partition matrix, $\mathbf{K}$, used in the *Reference* case evolves and reaches values associated to the solidus temperature.

Solute component	Cr	Fe	Nb	Mo	Ti	Al	C
Liquidus slope, $m_i^{bin}(T_L^{bin}(w_i^{bin}))$ [K wt.%$^{-1}$]	-1.815	-0.449	-5.559	0.145	-9.66	-0.26	-55.4
Segregation coefficient, $k_i^{bin}(T_L^{bin}(w_i^{bin}))$ [wt.% wt.%$^{-1}$]	0.934	0.982	0.659	1.014	0.633	0.991	0.208

Table 6: Liquidus slopes, $m_i^{bin}(T_L^{bin}(w_i^{bin}))$, and segregation coefficients, $k_i^{bin}(T_L^{bin}(w_i^{bin}))$, $(1 \le i \le N-1)$, computed at the liquidus temperature, $T_L^{bin}(w_i^{bin})$, for each binary phase diagram with nickel at composition, $w_i^{bin} = w_i^0$ $(1 \le i \le N-1)$, of the IN718 Ni-base superalloy composition (Tab. 1) for case *Multi-binary* (Tab. 3) [43].

4.2. Multi-binary phase diagram

The *Multi-binary* approach [28] uses thermodynamic properties estimated from the binary phase diagrams of each alloying elements with the main component. In this approach, the liquidus slopes, $m_i^{bin}(T_L^{bin}(w_i^{bin}))$, and segregation coefficients, $k_i^{bin}(T_L^{bin}(w_i^{bin}))$ $(1 \le i \le N-1)$, are extracted from the binary phase diagram of solute i with Ni at the nominal composition $w_i^{bin} = w_i^0$ and liquidus temperature $T_L^{bin}(w_i^{bin})$; hence, without consideration of the effects of the other elements. For the present alloy (Tab. 1), the resulting values are listed in Tab. 6. The current values show very large differences with those in Tab. 5, despite the use of the same database. For instance, the segregation coefficients are lower than unity for Cr and Fe and higher than unity for Mo, while opposite behaviour is found when evaluated at the liquidus temperature of the alloy, as in the *Multi-linear* case. Similarly, the slope at the liquidus temperature of the binary Ni - 3.1 wt % Mo alloy is $0.145\,\text{K wt.\%}^{-1}$, but is $-4.339\,\text{K wt.\%}^{-1}$ for IN718. Because the diffusion matrix and Gibbs-Thomson coefficient are the same as the *Reference* case, the differences in Fig. 8 are solely due to the use of m_i^{bin} and k_i^{bin}. For the *Multi-binary* approximation, the range of velocity for dendritic growth, $[v_c, v_a]$ (Tab. 4), drastically decreases and the radius increases for all velocities. The use of these binary parameters also has significant consequences on the dendrite tip undercooling, which does not exceed 30 K with this approximation. It is worth noting that this methodology results in the estimation of each binary phase-diagram property at a different temperature, as $\forall\, i \in \{1, N-1\}$, $T_L^{bin}(w_i^{bin}) \neq T_L^0(\mathbf{w}^0)$. Hence, this strategy is inadequate, regardless of the processing conditions.

4.3. Pseudo-binary alloy

The *Pseudo-binary* strategy consists of finding an equivalent binary alloy [27, 74], in which the multi-component phase diagram properties, but also the alloy composition and diffusion coefficient, have to be replaced by adequate single values. A clear advantage of this method is the ability to apply the well-established theories for binary alloys, e.g., the Kurz-Giovanola-Trivedi model [20], together with all the extensions that account for a non-equilibrium interface. Unlike the previous cases, cross-diffusion is necessarily neglected, but the Gibbs-Thomson coefficient of the *Reference* case is maintained. The equivalent composition of the *virtual* component, $\overline{w}$, is assumed to be the sum of the compositions of all solute components. The associated liquidus slope, $\overline{m}$, segregation coefficient, $\overline{k}$, and diffusion coefficient, $\overline{D}$, are estimated as averaged properties using the following expressions [26]:

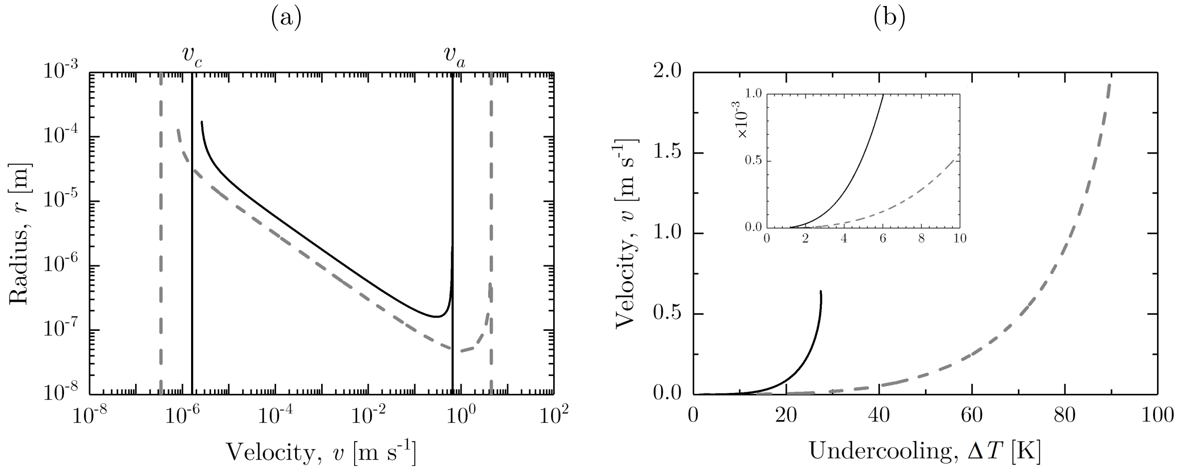

Figure 8: Dendrite tip kinetics comparing (thin plain lines) case *Multi-binary* (Tables 3 and 6) with (thick dashed lines) the *Reference* case to highlight the role of thermodynamic coupling when simplifying the phase diagram properties. Comparisons include (a) the tip radius versus velocity and (b) the undercooling versus velocity.

Property	Symbol	Equivalent value	Unit
Pseudo-binary alloy composition	$\overline{w^0}$	46.515	[wt.%]
Pseudo-binary liquidus slope	$\overline{m}$	-3.112	[K wt.%$^{-1}$]
Pseudo-binary segregation coefficient	$\overline{k}$	0.721	[wt.% wt.%$^{-1}$]
Pseudo-binary diffusion coefficient	$\overline{D}$	3.123×10^{-9}	[m^2 s^{-1}]

Table 7: Liquidus slopes, $\overline{m}$ (Eq. 25), and segregation coefficients, $\overline{k}$ (Eq. 25), composed from the computed (Tab. 2) liquidus slopes, $m_i(T_L, \mathbf{w}^0)$, and segregation coefficients, $k_i(T_L, \mathbf{w}^0)$ ($1 \leq i \leq N-1$), computed at the liquidus temperature, $T_L(\mathbf{w}^0)$, and composition, $\mathbf{w}^0$, of the IN718 Ni-base superalloy (Tab. 1) for case *Pseudo-binary* (Tab. 3), also including equivalent pseudo-binary composition, $\overline{w}$ (Eq. 25), and diffusion coefficient, $\overline{D}$ (Eq. 25) [43, 44].

$$\begin{aligned} \overline{w^0} &= \sum_{i=1}^{N-1} w_i^0 \qquad & \overline{m} &= \frac{1}{\overline{w}} \times \sum_{i=1}^{N-1} m_i\, w_i^0 \\ \overline{k} &= \frac{1}{\overline{m}\,\overline{w}} \times \sum_{i=1}^{N-1} k_i m_i\, w_i^0 \qquad & \overline{D} &= \frac{1}{\overline{w}} \times \sum_{i=1}^{N-1} D_{ii}\, w_i^0 \end{aligned} \tag{25}$$

The computed properties of the pseudo-binary alloy are provided in Tab. 7. The evolution of the dendrite tip radius, drawn in Fig. 9 (a), shows similar evolution to the *Reference* case on a large range of velocities, below 10^{-2} m s^{-1}. However, the evolution of growth velocity is clearly restricted with higher v_c and smaller v_a (4). A large departure from the *Reference* case is observed beyond 10^{-2} m s^{-1} for both the radius and the undercooling, the latter being underestimated for a given velocity. The underestimation of the undercooling is opposite of the *Multi-linear* case, and is simply due to the fact that the solidus temperature of the pseudo-binary phase diagram, at which v_a is reached, is reduced with the properties computed in Tab. 7. Within the velocity range $[10^{-6}, 10^{-2}]$ m s^{-1}, the agreement with the *Reference* case is remarkably accurate, and the *Pseudo-binary* approximation could thus be considered for some

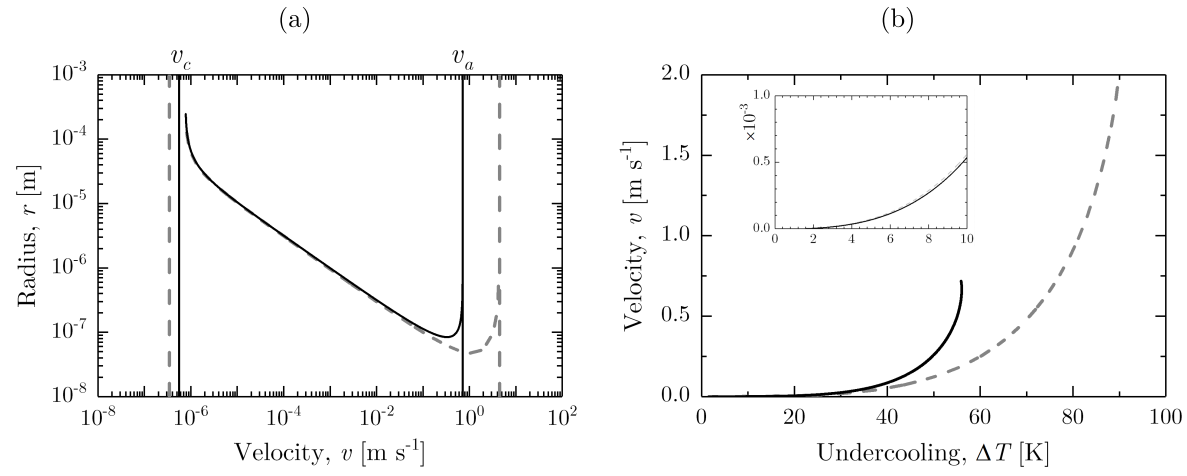

Figure 9: Dendrite tip kinetics comparing (thin plain lines) case *Pseudo-binary* (Tables 3 and 7) with (thick dashed grey lines) the *Reference* case to highlight the role of thermodynamic coupling when simplifying the phase diagram properties. Comparisons include (a) the tip radius versus velocity and (b) the undercooling versus velocity.

conventional casting simulations.

4.4. *Curvature approximation*

The influence of the Gibbs-Thomson coefficient on the growth kinetics of the dendrite tip is now investigated. The value previously estimated in *Reference* case from Fig. 4 (b) was the result of coupling with thermodynamic equilibrium calculations and inputting the interfacial energy for pure nickel [53, 54]. Values of the Γ coefficient are also directly reported in literature for solidification studies of IN718: 1.4×10^{-7} K m [75], 1.8×10^{-7} K m [76] or 3.65×10^{-7} K m [77]. However, a careful reading of these papers shows that these estimations are not associated to IN718 and/or seem inadequately justified by their authors. In this case, we quantify the effect of the Gibbs-Thomson coefficient using the value reported for pure nickel, $\Gamma_{Ni} = 1.91 \times 10^{-7}$ K m [49] (Tab. 2).

Fig. 10 (a) shows a slightly lower estimation of the tip radius with an increase of the absolute stability velocity (Tab. 4). Despite a large difference in Gibbs-Thomson coefficient, only slight differences are observed in the evolution of growth velocity at large undercooling, i.e., greater than 20 K, as shown in Fig. 10 (b). The differences are better visualized at low undercooling, $\Delta T \leq 10$ K, in the inserted sub-figure, demonstrating the increase in growth velocity expected when decreasing the Gibbs-Thomson coefficient. This increase is inversely proportional to the one associated to Γ value ($\Gamma/\Gamma_{Ni} \simeq 1.76$). The full diffusion matrix and the approximation of the phase diagram using the *Multi-linear* case are maintained in this study (Tab. 3), so it is possible to compare the results at high undercoolings to the *Multi-linear* case, as displayed in Fig. 7. One can observe that the underestimation of the velocity at high undercooling shown in Fig. 7 for the *Multi-linear* case is not retrieved in Fig. 10 for the *Curvature* case. In fact, the decrease of the Gibbs-Thomson coefficient is counteracted by the decrease of the tip radius at high velocity, resulting in an increase of the total curvature undercooling. Finally, one can see that v_a naturally increases, as it is inversely proportional to the Gibbs-Thomson coefficient (Eq. 23, Tab

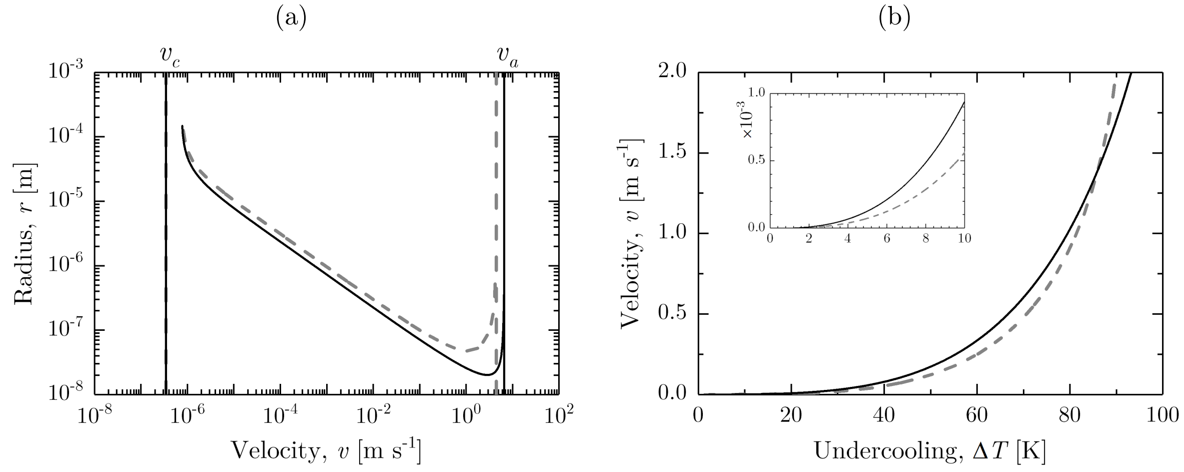

Figure 10: Dendrite tip kinetics comparing (thin plain lines) case *Curvature* (Table 3, using Γ_{Ni} from Table 2) with (thick dashed grey lines) the *Reference* case to highlight the role of the Gibbs-Thomson coefficient. Comparisons include (a) the tip radius versus velocity and (b) the undercooling versus velocity.

4).

4.5. Diagonal diffusion matrix

The role of the diffusion matrix, $\mathbf{D}$, is now investigated to highlight the influence of the diffusional interactions. This was done in previous contributions and is a good methodology to evaluate quantitative deviation from a reference solution [78, 10], validate or invalidate existing theories [79], and to verify that the results retrieve the most-commonly available solutions for a diagonal matrix. In this case, the diffusion matrix is simply restricted to its single-diagonal terms, leading a pure diagonal form, $\mathbf{D_{diag}} = (D_{ij}\,\delta_{ij})_{1\leq(i,j)\leq N-1}$. As before, this is done while maintaining the linearized phase diagram properties of the *Multi-linear* case, allowing the two cases to be compared. Small differences are observed between the *Multi-linear* and *Diagonal diffusion* cases when comparing Figs 7 and 11. Deviations from the *Reference* case are of the same nature as explained in Section 4.1, i.e., due to the constant values of the phase-diagram properties in the solidification interval. The fact that velocities v_c and v_a are not significantly changed (Tab. 4) indicates that the cross-diffusion terms are of little influence in Eqs. (19) and (23). Of course, this comment should not be immediately generalized to other systems.

4.6. Non-equilibrium interface

The last study investigates the effects of interfacial non-equilibrium due to rapid solidification. At large interfacial velocities, local thermodynamic equilibrium can no longer be maintained. This results in a departure of the interfacial temperature and compositions from those given by the phase diagram, and thus must affect the growth rate and compositions of the growing dendrite and composition fields in the liquid. In addition, these non-equilibrium effects will alter the stability analysis used to compute the tip radius [80, 81]. A full treatment of the effects of non-equilibrium interfacial processes is beyond the scope of this paper. However, to illustrate the potential effects of non-equlibrium solidification, we

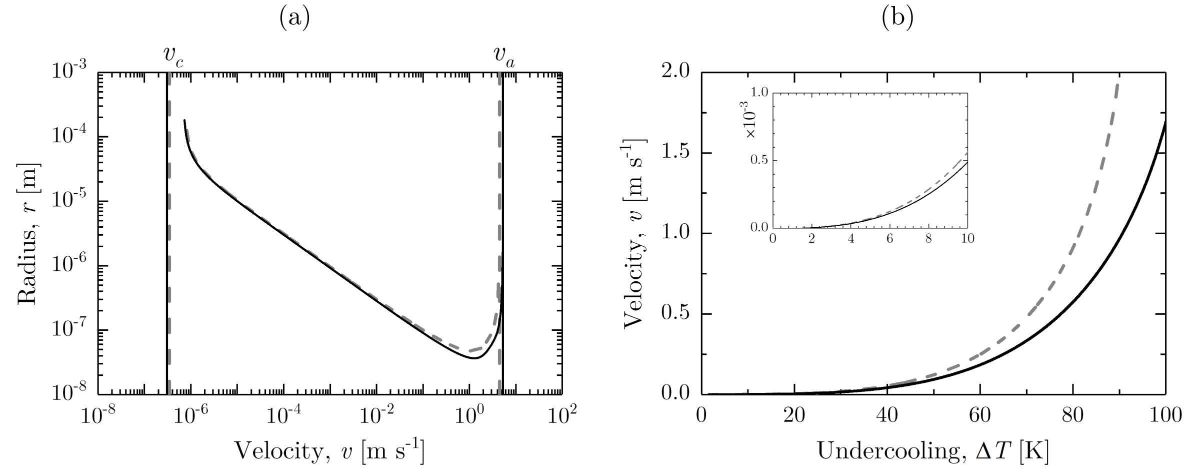

Figure 11: Dendrite tip kinetics comparing (thin plain lines) case *Diagonal diffusion* (Tab. 3) with (thick dashed grey lines) the *Reference* case to highlight the role of the diffusion matrix. Comparisons include (a) the tip radius versus velocity and (b) the undercooling versus velocity.

employ the strong approximations that the phase boundaries are linear, there is no solute drag at the interface, and a simple model for solute trapping holds. In addition, to determine the tip radius, we use the stability analysis given above with the values of the non-equilibrium interfacial compositions and temperature. This neglects, for example, the possibility of oscillatory instabilities, and the full coupling of these velocity-dependent terms to the growth rate of the instability. We follow the developments by Aziz [21] and Boettinger and Coriell [66], in which a kinetic contribution proportional to the interface velocity, ΔT_ζ, is added to the total undercooling in Eq. (14a) [1], giving:

$$\Delta T = \Delta T\chi + \Delta T\kappa + \Delta T_\zeta \tag{26}$$

$$\Delta T_\zeta = \frac{R\,T_L}{\Delta S_f}\frac{v}{v_0} \tag{27}$$

where R is the gas constant, ΔS_f is the entropy of fusion per mole, computed at the liquidus temperature of the alloy [43], and v_0 is the maximum velocity at which crystallization can occur [1]. This velocity is not known for IN718, and only indirect estimations may be proposed. The sound velocity in metals ($\approx 1000\,\mathrm{m\,s^{-1}}$) is presented as an upper limit, but lower estimations are reported [82, 83].

Additionally, the interfacial compositions are now dependent on velocity, which is described in dilute-ideal thermodynamic systems with analytical expressions for the non-equilibrium segregation coefficients, $k_i^v \equiv k_i(T_L, \mathbf{w}^0, v)$ and liquidus slopes, $m_i^v \equiv m_i(T_L, \mathbf{w}^0, v)$, $(1 \leq i \leq N-1)$ for all i-solute components:

$$k_i^v = \frac{k_i + \delta\,v/D_i^{int}}{1 + \delta\,v/D_i^{int}} \tag{28}$$

$$m_i^v = m_i\frac{1 - k_i^v + k_i^v \ln\left(k_i^v/k_i\right)}{1 - k_i} \tag{29}$$

Property	Symbol	Value	Unit
Diffusion coefficient over interface width	D_i^{int}/δ	1	[m s^{-1}]
Crystallization velocity	v_0	1000	[m s^{-1}]
Melting entropy [43]	ΔS_f	9.1016	[J mol^{-1} K^{-1}]
Gas constant [84]	R	8.314	[J mol^{-1} K^{-1}]

Table 8: Physical and thermodynamic properties associated to *Non-equilibrium* interface assuming solute trapping with segregation coefficients, $k_i(T_L, \mathbf{w}^0, v)$ $(1 \leq i \leq N-1)$ (Eq. 28), and liquidus slopes, $m_i(T_L, \mathbf{w}^0, v)$ $(1 \leq i \leq N-1)$ (Eq. 29) for case *Non-equilibrium* interface [21, 66].

where the equilibrium phase diagram parameters, $m_i \equiv m_i(T_L, \mathbf{w}^0)$ and $k_i \equiv k_i(T_L, \mathbf{w}^0)$ are given by the *Multi-linear* case (Tab. 5). The parameter $\delta\, v/D_i^{int}$ in Eq. (28) can be considered as an interfacial Péclet number, where δ is a characteristic interface width and D_i^{int} is the diffusion coefficient for element i within the interface. Here, we assume identical estimations of the D_i^{int}/δ ratio for all solute components. Tab. 8 presents the additional properties used in this case to account for an interface that departs from thermodynamic equilibrium.

Fig. 12 highlights the kinetic effects on the radius and undercooling. As expected, no difference is found at low velocity, as kinetic effects will be negligible at small velocities. Consequently, the results are similar to those ones presented in Fig. 7 (a), as this case also considers the full diffusion matrix for solute diffusion. As already discussed, these results are close to the *Reference* case at low velocity. When velocity is increased, clear differences are observed, and the interface is stabilized at an absolute velocity considerably lower than the *Reference* case (Tab. 4).

The absolute velocity is also estimated from the solution of the non-linear system of Eqs. (23,28,29), but using the non-equilibrium partition coefficients and liquidus slopes. In Fig. 12 (b), a decrease of the tip undercooling is even predicted when approaching planar front growth. This effect is also reported by Kurz and Trivedi [85] and would play a role in explaining the formation of banded structures at high velocities. Hence, accounting for interface non-equilibrium effects lowers the growth undercooling despite the addition of a kinetic contribution, ΔT_ζ. In fact, the kinetic contribution remains very small, considering the properties listed in Tab. 8, and the main effect on the undercooling is due to the reduction of solute segregation. As described by Eq. (28), the coefficients $k_i(T_L, \mathbf{w}^0, v)$ $(1 \leq i \leq N-1)$ tend toward unity as the velocity increases, which significantly reduces the chemical contribution to the undercooling, ΔT_χ. It was verified that all segregation coefficients computed by Eq. 28 asymptotically approach unity; however, in the present situation, one can observe that $v_a = 0.678\,\mathrm{m\,s^{-1}}$ (Tab. 4) is lower than the ratio D_i^{int}/δ for all solute components (Tab. 8), resulting in moderate solute trapping at v_a. Although solute trapping is a well-established phenomenon, Fig. 5 (a) shows that the partition coefficient computed at interfacial equilibrium, particularly that for Al in this case, may increase as the interfacial compositions move along the nonlinear phase diagram. Even if the phase diagram is linear, the segregation coefficient may change as the tie line evolves with changes in the diffusion coefficients of the solute species. Thus, it may be incorrect to attribute an observed increase in partition coefficient with velocity entirely to kinetic effects, as thermodynamic effects can also contribute when considering the full phase diagram and diffusion matrix.

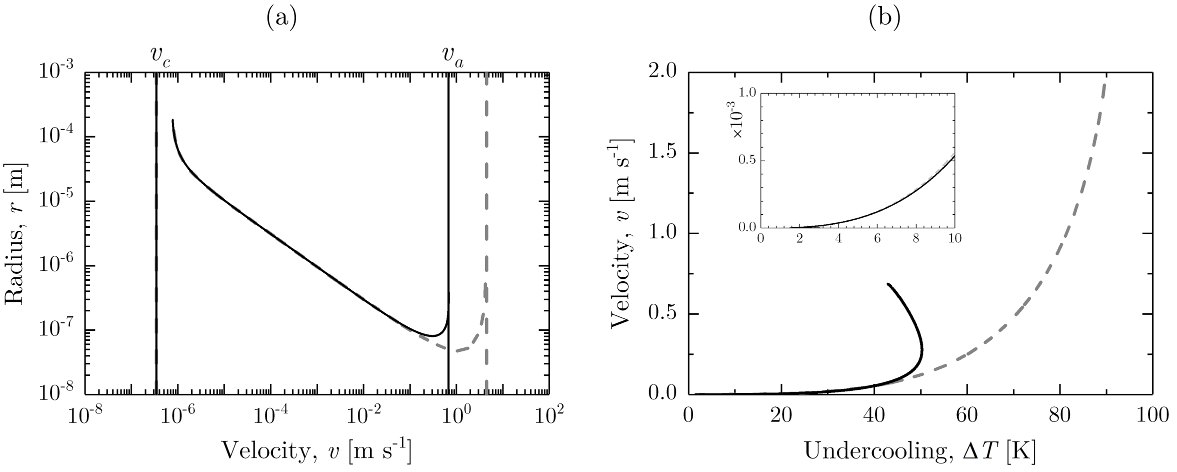

Figure 12: Dendrite tip kinetics comparing (thin plain lines) case *Non-equilibrium* interface (Tables 3 and 8) with (thick dashed grey lines) the *Reference* case to highlight the role of solute trapping [21]. Comparisons include (a) the tip radius versus velocity and (b) the undercooling versus velocity.

5. Conclusion

A model of dendrite tip growth kinetics coupled with thermodynamic equilibrium calculations has been developed and presented. This model builds on Hunziker's multicomponent theory [10] and generalizes it further by removing the assumptions of a diagonal partition matrix and constant thermodynamic properties. Additionally, expressions to calculate the velocity domain, $[v_c, v_a]$, corresponding to the limits of stability of a planar front, have been introduced. The model is applied to the IN718 nickel-base superalloy while fixing the temperature gradient, G, covering the whole solidification temperature range, i.e., from the liquidus temperature to the solidus temperature, and from $v_c = 3.441 \times 10^{-7}\,\mathrm{m\,s^{-1}}$ and $v_a = 4.379\,\mathrm{m\,s^{-1}}$. The Gibbs-Thomson coefficient, Γ, is extracted from this application. The discussion of the results is then organized to compare the present model, serving as a *Reference* case, with classical approaches that do not use iterative thermodynamic equilibrium calculations to find the working point of the dendrite tip. The following observations can be made:

- *Multi-linear* phase diagram approximations: Using constant values of the segregation coefficients and liquidus slopes calculated at the liquidus temperature of the alloy provides good results for velocities below $0.1\,\mathrm{m\,s^{-1}}$. A deviation from the reference calculation occurs at high velocities, as although the tip temperature decreases, the thermodynamic properties are no longer equal to the values at the liquidus temperature. Using this same approximation while neglecting the off-diagonal terms of the diffusion matrix in the liquid gives very similar results (case *Diagonal*), indicating little dependence of the effects of cross-diffusion on the solute components in the liquid on the dendrite tip kinetics, despite the existence of non-monotonic diffusion profiles (Fig. 6). Additionally, with the phase diagram approximations, modifying the Gibbs-Thomson coefficient by a factor of 1.76

decreases the tip radius but increases the curvature undercooling, hence leading to very similar results (case *Curvature*). The constitutional supercooling velocity, v_c, is not modified by these changes, while the absolute velocity for stability, v_a, is, as the latter is a direct function of the segregation coefficient at the solidus temperature and the Gibbs-Thomson coefficient.

- Use of binary phase diagrams: This common approximation, which consists of using the binary phase diagrams for the solvent and a single solute component to estimate the properties of the multicomponent phase diagram (case *Multi-Binary*), reveals itself to be the least accurate methodology in comparison with the reference solution. Surprisingly, building a *Pseudo-binary* phase diagram using the set of Eqs. 25 is in much better agreement with the reference solution at low velocities, below $1 \times 10^{-2}\,\mathrm{m\,s^{-1}}$. However, the absolute stability velocity is drastically underestimated.
- *Non-equilibrium* condition at the solid-liquid interface: This condition is tested by introducing velocity dependence to the equilibrium segregation coefficients and liquidus slope deduced from the *Multi-linear* approximation. This velocity dependence is based on expressions proposed for ideal-dilute thermodynamic solutions [21, 66]. As expected, the results are superimposed on the reference solution at low velocities where the phase-diagram properties are not modified, but diverge from the reference solution at high velocities when the segregation coefficients of all species tend toward unity and the solidification interval progressively vanishes as the liquidus and solidus slopes tend toward the same value.

Coupling the growth model with updates of thermodynamic equilibrium calculations is shown to be necessary at high growth velocities, but non-equilibrium effects could become dominant when the Péclet number at the interface increases. This clearly motivates future developments, as a model of dendrite growth kinetics coupled with prediction of non-equilibrium effects for multicomponent alloys is required at high velocities, but cannot be satisfied by the approximations given through Eqs. (27,28,29) [21, 66, 1]. Thus, the next step of the present work would incorporate calculations of non-equilibrium effects, considering both solute trapping and solute drag, following the methodology developed by Aziz and Kaplan [67]. Removing the ideal-solution assumptions and coupling the non-equilibrium effects with the equations given in Section 2 will then provide a more general framework for computation of the dendrite tip kinetics for multicomponent alloys. Additional coupling with databases of thermophysical properties could also be implemented, which includes coupling with predicted variations of the interface energy with interface composition and temperature. This model would be useful for the interpretation of experiments conducted at high velocity, e.g., solidification of the undercooled systems found in atomization or levitated droplet experiments [86, 87, 88], as well as for the prediction of dendrite growth kinetics during rapid solidification processes such as additive manufacturing [89, 90].

Data availability

All data included in this study are available upon reasonable request by contact with the corresponding author.

Declaration of competing interest

The authors declare that they have no known competing financial interests or personal relationships that could have appeared to influence the work reported in this paper.

Acknowledgments

CAH acknowledges support from the National Science Foundation Graduate Research Fellowship (grant number DGE-1842165), and from the Ryan Fellowship at the International Institute for Nanotechnology. PWV acknowledges the financial assistance award 70NANB14H012 from the U.S. Department of Commerce, National Institute of Standards and Technology as part of the Center for Hierarchical Materials Design (CHiMaD). CAG was supported by the European Space Agency (Noordwijk, NL) under the project NEQUISOL (contract number 15236/02/NL/SH).

Nomenclature

Latin symbols

C	Parameter for solute composition profile	wt.%
D_i	Diffusion coefficient for element i in the liquid phase	$\mathrm{m}^2\ \mathrm{s}^{-1}$
G	Temperature gradient	$\mathrm{K\ m}^{-1}$
G_χ	Solute gradient at the $s\backslash l$ interface	$\mathrm{wt.\%\ m}^{-1}$
J_i	Diffusion flux of the solute specie i	$\mathrm{kg\ m}^{-2}\ \mathrm{s}^{-1}$
k	Segregation coefficient	$\mathrm{wt.\%\ wt.\%}^{-1}$
m	Liquidus slope	$\mathrm{K\ wt.\%}^{-1}$
n	Iteration number	–
N	Number of chemical elements in the alloy	-
Pe	Péclet number	-
r	Curvature radius	m
R	Gas constant	$\mathrm{J\ mol}^{-1}\ \mathrm{K}^{-1}$
t	Time	s
T	Temperature	K
v	Dendrite growth velocity	$\mathrm{m\ s}^{-1}$
v_c	Critical velocity (*Constitutional supercooling criterion*)	$\mathrm{m\ s}^{-1}$
v_a	Velocity of absolute stability	$\mathrm{m\ s}^{-1}$
v_0	Limit velocity at which crystallisation occurs	$\mathrm{m\ s}^{-1}$
V_M	Molar volume	$\mathrm{m}^3\ \mathrm{mol}^{-1}$
w	Mass composition	wt.%
x, y, z	Cartesian coordinates	m
$\widetilde{X}$	Coefficient used for v_a estimation	$\mathrm{wt.\%\ m}^2\ \mathrm{s}^{-1}$
$\mathbf{A}$	A coefficients vector	wt.%
$\mathbf{B}$	Eigenvalues vector of the diffusion matrix	$\mathrm{m}^2\ \mathrm{s}^{-1}$
$\mathbf{D}$	Diffusion matrix in the liquid phase	$\mathrm{m}^2\ \mathrm{s}^{-1}$
$\mathbf{F}$	F coefficients vector	$\mathrm{wt.\%\ m}^{-1}$

$\mathbf{K}$	Partition matrix	wt.% wt.%$^{-1}$
$\mathbf{U}_{.\mathbf{j}}$	Unit eigenvectors of the diffusion matrix	–

Greek symbols

γ	Interfacial energy	J m^{-2}
Γ	Gibbs-Thomson coefficient	K m
δ	Characteristic interface width	m
ΔG^s_κ	Gibbs energy induced by curvature effect	J m^{-3}
ΔS_f	Entropy of fusion	J mol^{-1} K^{-1}
ΔT	Undercooling at dendrite tip	K
ΔT_0	Solidification interval	K
Δw	Difference in interfacial composition	wt.%
ζ	Velocity factor	-
κ	Curvature	m^{-1}
λ_{min}	Minimum unstable wavelength	m
ξ,η	Paraboloidal coordinates	-
ξ	Correction factor	-
σ	Selection constant	-
ρ	Density	kg m^{-3}
ω	Wavenumber	m^{-1}
Ω	Supersaturation	-

Superscripts

0	Nominal value
l	Liquid phase
sl	In solid at solid-liquid interface
ls	In liquid at solid-liquid interface
(n)	Iteration
s	Solid phase
v	velocity effect on thermodynamic properties

Subscripts

i, j, k, l	Chemical component
$diag$	Diagonal
L	Liquidus
S	Solidus
κ	Curvature effect
χ	Chemical effect
ζ	Kinetic effect

Mathematical notations

$\mathrm{E}_1(.)$	Exponential integral function
$\mathrm{F}_{\mathrm{L}}(.)$	Function associated to liquidus temperature computation
$\mathrm{F}_{\mathrm{S}}(.)$	Function associated to solidus temperature computation
$\mathrm{F}_{\mathrm{W}^{\mathrm{S}}}(.)$	Function associated to composition in solid phase
$\mathrm{F}_{\mathrm{V}_{\mathrm{M}}}(.)$	Function associated to molar volume computation
$\mathrm{Iv}(.)$	Ivantsov function
$\delta_{..}$	Kronecker symbol

Appendices

A. Diffusion and partition matrices

The present appendix gathers the values of the diffusion matrix for all solute components of the IN718 nickel-base superalloy computed at the liquidus temperature, **D**, its eigenvalues, **B**, the corresponding transformation matrix, **U**, and its eigenvectors, $\mathbf{U_{\cdot j}}$, as well as the partition matrix, **K**, computed at the solidus temperature [43, 44].

$$\mathbf{D} = \begin{array}{cccccccc} & \text{Cr} & \text{Fe} & \text{Nb} & \text{Mo} & \text{Ti} & \text{Al} & \text{C} \\ \text{Cr} & 3.4890 & 0.2957 & 1.8483 & 0.4767 & 3.6253 & 2.4718 & -3.2768 \\ \text{Fe} & 0.0952 & 2.9709 & 1.0524 & 1.1992 & 1.7052 & 0.5037 & 0.2597 \\ \text{Nb} & 0.4470 & 0.3571 & 3.5689 & 0.2119 & 1.1756 & 0.7859 & -1.1443 \\ \text{Mo} & 0.0027 & 0.0365 & -0.0024 & 1.0830 & 0.1128 & 0.1105 & -0.1021 \\ \text{Ti} & 0.3103 & 0.2203 & 0.4643 & 0.3064 & 3.3502 & 0.3632 & -0.2992 \\ \text{Al} & 0.1077 & 0.0536 & 0.1551 & 0.1383 & 0.1736 & 2.9085 & 0.1637 \\ \text{C} & -0.0981 & -0.0279 & -0.1779 & -0.1050 & -0.1437 & 0.0721 & 9.2121 \end{array} \times 10^{-3}\,\mathrm{mm}^2\,\mathrm{s}^{-1}$$

Table 9: Diffusion matrix, **D**, in liquid phase of the IN718 nickel-base superalloy computed at liquidus temperature, T_L (Tab. 2) [43, 44].

$$\begin{array}{cccccccc} & \#1 & \#2 & \#3 & \#4 & \#5 & \#6 & \#7 \\ \hline \mathbf{B} = & 9.351 & 5.589 & 3.031 & 2.790 & 2.676 & 2.099 & 1.045 \end{array} \times 10^{-3}\,\mathrm{mm}^2\,\mathrm{s}^{-1}$$

$$\mathbf{U} = \begin{array}{cccccccc} & \#1 & \#2 & \#3 & \#4 & \#5 & \#6 & \#7 \\ \#1 & 566 & 811 & -642 & -549 & 337 & 773 & -26.1 \\ \#2 & 37.9 & 362 & 754 & 63.2 & -775 & 572 & 490 \\ \#3 & 220 & 383 & 115 & 612 & 480 & -168 & -45.4 \\ \#4 & 11.1 & 9.91 & 9.52 & -7.52 & -40.3 & -7.55 & -866 \\ \#5 & 87.4 & 235 & 6.33 & -449 & -91.2 & -208 & 71.8 \\ \#6 & -2.37 & 80.9 & -71.8 & 343 & -216 & -63.5 & 49.6 \\ \#7 & -789 & 51.6 & -2.32 & -5.19 & 14.5 & 5.01 & -9.93 \end{array} \times 10^{-3}$$

Table 10: Set of $N-1=7$ eigenvalues, B_j, and transformation matrix, **U**, with unit eigenvectors, $\mathbf{U_{\cdot j}}$, of components, U_{ij}, associated to the diffusion matrix, **D**.

$$\mathbf{K} = \begin{array}{cc} & \begin{array}{ccccccc} \mathrm{Cr} & \mathrm{Fe} & \mathrm{Nb} & \mathrm{Mo} & \mathrm{Ti} & \mathrm{Al} & \mathrm{C} \end{array} \\ \begin{array}{c} \mathrm{Cr} \\ \mathrm{Fe} \\ \mathrm{Nb} \\ \mathrm{Mo} \\ \mathrm{Ti} \\ \mathrm{Al} \\ \mathrm{C} \end{array} & \begin{pmatrix} 1.11561 & -0.00502 & 0.13827 & 0.10589 & 0.22530 & -1.28927 & -3.72173 \\ 0.02422 & 1.25449 & 0.17006 & 0.14458 & 0.19923 & -0.71116 & 0.81223 \\ -0.12618 & -0.08750 & 0.51435 & -0.07413 & 0.17620 & 0.19274 & -0.91842 \\ 0.01894 & -0.01563 & -0.03118 & 0.69480 & 0.06113 & -0.23015 & -1.04000 \\ -0.02765 & -0.01591 & 0.01664 & -0.00001 & 0.59232 & 0.06476 & 0.14287 \\ -0.00141 & -0.00287 & 0.00967 & 0.00459 & 0.00818 & 1.57365 & 0.26691 \\ -0.00066 & -0.00017 & -0.00043 & -0.00031 & 0.00022 & 0.00842 & 0.09409 \end{pmatrix} \end{array}$$

Table 11: Partition matrix, $\mathbf{K}$, between solid (s) and liquid (l) phases of the IN718 nickel-base superalloy at solidus temperature, T_S (Tab. 2) [43].

$$\mathbf{K} = \begin{array}{cc} & \begin{array}{ccccccc} \mathrm{Cr} & \mathrm{Fe} & \mathrm{Nb} & \mathrm{Mo} & \mathrm{Ti} & \mathrm{Al} & \mathrm{C} \end{array} \\ \begin{array}{c} \mathrm{Cr} \\ \mathrm{Fe} \\ \mathrm{Nb} \\ \mathrm{Mo} \\ \mathrm{Ti} \\ \mathrm{Al} \\ \mathrm{C} \end{array} & \begin{pmatrix} 1.05271 & 0.00047 & 0.18704 & 0.07340 & 0.47958 & -0.15624 & -3.89266 \\ 0.03423 & 1.14298 & 0.25249 & 0.10221 & 0.42590 & -0.15650 & 0.72526 \\ -0.05719 & -0.03008 & 0.40262 & -0.03580 & 0.04493 & 0.04120 & -0.44431 \\ 0.00514 & -0.01306 & -0.01822 & 0.74071 & 0.06122 & -0.02483 & -0.75151 \\ -0.01197 & -0.00581 & 0.00628 & -0.00078 & 0.46652 & 0.00475 & 0.01851 \\ -0.00251 & -0.00257 & 0.00720 & 0.00184 & 0.00410 & 0.95981 & 0.23341 \\ -0.00006 & 0.00001 & -0.00007 & -0.00002 & -0.00003 & 0.00076 & 0.10119 \end{pmatrix} \end{array}$$

Table 12: Partition matrix, $\mathbf{K}$, between solid (s) and liquid (l) phases of the IN718 nickel-base superalloy at liquidus temperature, T_L (Tab. 2) [43].

References

[1] W. Kurz, D. J. Fisher, Fundamentals of Solidification, Fourth Revised Edition, Trans Tech Publications Ltd, 1998.

[2] J. A. Dantzig, M. Rappaz, Solidification, 2nd Edition - Revised & Expanded, Coll. Materials, EPFL Press, 2016.

[3] W. Kurz, D. Fisher, R. Trivedi, Progress in modelling solidification microstructures in metals and alloys: dendrites and cells from 1700 to 2000, International Materials Reviews 64 (6) (2019) 311–354.

[4] W. Kurz, M. Rappaz, R. Trivedi, Progress in modelling solidification microstructures in metals and alloys. part ii: dendrites from 2001 to 2018, International Materials Reviews 66 (1) (2021) 30–76.

[5] W. A. Tiller, K. A. Jackson, J. W. Rutter, B. Chalmers, The redistribution of solute atoms during the solidification of metals, Acta Metallurgica 1 (4) (1953) 428–437.

[6] W. W. Mullins, R. F. Sekerka, Stability of a planar interface during solidification of a dilute binary alloy, Journal of Applied Physics 35 (1964) 444.

[7] R. Trivedi, W. Kurz, Morphological stability of a planar interface under rapid solidification conditions, Acta Metallurgica 34 (8) (1986) 1663–1670.

[8] D. Coates, S. Subramanian, G. R. Purdy, Solid-liquid interface stability during solidification of dilute ternary alloys, Transactions of the Metallurgical Society of AIME 242 (1968) 800.

[9] M. Bobadilla, J. Lacaze, L. G., influence des conditions de solidification sur le déroulement de la solidification des aciers inoxydables austénitiques, Journal of Crystal Growth 89 (1988) 531—544.

[10] O. Hunziker, Theory of plane front and dendritic growth in multicomponent alloys, Acta Materialia 49 (20) (2001) 4191–4203. `doi:https://doi.org/10.1016/S1359-6454(01)00313-5`.

[11] A. Papapetrou, Untersuchungen über dendritisches wachstum von kristallen, Zeitschrift für Kristallographie 92 (1935) 89–130.

[12] G. P. Ivantsov, Temperature field around a spherical, cylindrical, and needle-shaped crystal, growing in a pre-cooled melt, Dokl. Akad. Nauk SSSR 58 (4) (1947) 567–569.

[13] J. S. Langer, Dendrites, viscous fingers, and the theory of pattern formation, Science 243 (4895) (1989) 1150–1156.

[14] R. F. Sekerka, R. G. Seidensticker, D. R. Hamilton, J. D. Harrison, Investigation of desalinization by freezing, Westinghouse Research Lab. Report, Ch. 3 (1967).

[15] R. Trivedi, Growth of dendritic needles from a supercooled melt, Acta Metallurgica 18 (1970) 287–296.

[16] G. F. Bolling, W. A. Tiller, Growth from the melt. iii. dendritic growth, Journal of Applied Physics 32 (1961) 2587.

[17] J. S. Langer, H. Müller-Krumbhaar, Stability effects in dendritic crystal growth, Journal of Crystal Growth 42 (1977) 11–14.

[18] M. Glicksman, R. Schaefer, J. Ayers, Dendritic growth – a test of theory, Metallurgical Transactions A 7 (1976) 1747–1759.

[19] J. S. Langer, H. Müller-Krumbhaar, Theory of dendritic growth, Acta Metallurgica 26 (11) (1978) 1681–1708.

[20] W. Kurz, B. Giovanola, R. Trivedi, Theory of microstructural development during rapid solidification, Acta metallurgica 34 (5) (1986) 823–830.

[21] M. J. Aziz, Model for solute redistribution during rapid solidification, Journal of Applied Physics 53 (2) (1982) 1158–1168.

[22] J. S. Langer, Existence of needle crystals in local models of solidification, Physical Review A 33 (1) (1986) 435 – 441.

[23] D. A. Kessler, J. Koplik, H. Levine, Pattern selection in fingered growth phenomena, Advances in Physics 37 (3) (1988) 255–339. `doi:10.1080/00018738800101379`.

[24] P. Pelcé, Dynamics of Curved Fronts, 1st Edition, Academic Press, 1988.

[25] E. Brener, V. Mel'nikov, Pattern selection in two-dimensional dendritic growth, Advances in Physics 40 (1) (1991) 53–97. `doi:10.1080/00018739100101472`.

[26] A. Kermanpur, M. Rappaz, N. Varahram, P. Davami, Thermal and grain-structure simulation in a land-based turbine blade directionally solidified with the liquid metal cooling process, Metallurgical and Materials Transactions B 31 (2000) 1293–1304. `doi:https://doi.org/10.1007/s11663-000-0017-z`.

[27] S. Raghavan, G. Singh, S. Sondhi, S. Srikanth, Construction of a pseudo-binary phase diagram for multi-component ni-base superalloys, Calphad 38 (2012) 85–91. `doi:https://doi.org/10.1016/j.calphad.2012.04.003`.

[28] C.-A. Gandin, M. Rappaz, , R. Tintiller, Three-dimensional probabilistic simulation of solidification grain structures: Application to superalloy precision castings, Metallurgical Transactions A 24A (1993) 467–479.

[29] P. Gilgien, Calcul de cartes de microstructures de solidification pour le système Al-Fe-Si, Ph.D. thesis, LSMX - Laboratoire de simulation des matériaux, EPFL (1996). `doi:10.5075/epfl-thesis-1465`.

[30] R. Zhang, X. Wang, Z. Chen, W. Jie, Simulation of constrained dendrite growth of multicomponent alloys using a calphad method, Materials Science and Technology 20 (2) (2004) 181–184.

[31] K. Wang, H. Wang, F. Liu, H. Zhai, Modeling dendrite growth in undercooled concentrated multi-component alloys, Acta Materialia 61 (11) (2013) 4254–4265. `doi:https://doi.org/10.1016/j.actamat.2013.03.051`.

[32] A. Lahiri, A. Choudhury, Dendrite tip selection during isothermal free growth in multi-component alloys: Marginal stability theories and insights from phase-field simulations,, Computational Materials Science 158 (2019) 209–218.

[33] J. Liu, J. Zou, M. Guo, N. Moelans, Phase-field simulation and analytical modelling of casio3 growth in cao-al2o3-sio2 melts, Computational Materials Science 144 (2018) 126–132. `doi:https://doi.org/10.1016/j.commatsci.2017.12.018`.

[34] M. Abramowitz, I. Stegun, Handbook of Mathematical Functions - Tenth printing, National Institute of Standards and Technology, 1972.

[35] Thermocalc software, Thermo-Calc Software AB, Sweden (2021).
URL `https://thermocalc.com`

[36] Y. Ma, J. Sun, X. Xie, Y. Hu, J. Zhao, P. Yan, An investigation on fine-grain formation and structural character in cast in718 superalloy, Journal of Materials Processing Technology 137 (1) (2003) 35–39, iUMRS BB. `doi:https://doi.org/10.1016/S0924-0136(02)01063-4`.

[37] D. Dye, O. Hunziker, R. Reed, Numerical analysis of the weldability of superalloys, Acta Materialia 49 (4) (2001)

683–697. doi:https://doi.org/10.1016/S1359-6454(00)00361-X.

[38] V. Patel, A. Sali, J. Hyder, M. Corliss, D. Hyder, W. Hung, Electron beam welding of inconel 718, Procedia Manufacturing 48 (2020) 428–435, 48th SME North American Manufacturing Research Conference, NAMRC 48. doi:https://doi.org/10.1016/j.promfg.2020.05.065.

[39] H. Lv, X. Li, Z. Li, W. Wang, K. Yang, F. Li, H. Xie, Investigation on the columnar-to-equiaxed transition during laser cladding of in718 alloy, Journal of Manufacturing Processes 67 (2021) 63–76. doi:https://doi.org/10.1016/j.jmapro.2021.04.016.

[40] Z. Wang, K. Guan, M. Gao, X. Li, X. Chen, X. Zeng, The microstructure and mechanical properties of deposited-in718 by selective laser melting, Journal of Alloys and Compounds 513 (2012) 518–523.

[41] A. Queva, G. Guillemot, C. Moriconi, C. Metton, M. Bellet, Numerical study of the impact of vaporisation on melt pool dynamics in laser powder bed fusion - application to in718 and ti–6al–4v, Additive Manufacturing 35 (2020) 101249. doi:https://doi.org/10.1016/j.addma.2020.101249.

[42] D. Zhang, Z. Feng, C. Wang, W. Wang, Z. Liu, W. Niu, Comparison of microstructures and mechanical properties of inconel 718 alloy processed by selective laser melting and casting, Materials Science and Engineering: A 724 (2018) 357–367. doi:https://doi.org/10.1016/j.msea.2018.03.073.

[43] Thermocalc database TCNI10 \Ni-Alloys v10.0, Thermo-Calc Software AB, Sweden (2021).
URL https://thermocalc.com

[44] Thermocalc database MOBNI5 \Ni-Alloys Mobility v5.1 , Thermo-Calc Software AB, Sweden (2021).
URL https://thermocalc.com

[45] C. E. Campbell, W. J. Boettinger, U. R. Kattner, Development of a diffusion mobility database for Ni-base superalloys, Acta Materialia 50 (2002) 775–792.

[46] T. Zykova-Timan, R. Rozas, J. Horbach, K. Binder, Computer simulation studies of finite-size broadening of solid-liquid interfaces: from hard spheres to nickel, J. Phys.: Condens. Matter 21 (2009) 464102. doi:https://doi.org/10.1016/j.jmapro.2021.04.016.

[47] Z. Jian, K. Kuribayashi, W. Jie, Solid-liquid interface energy of metals at melting point and undercooled state, Materials Transactions 43 (2002) 721–726.

[48] F. Luo, X.-R. Chen, L.-C. Cai, G.-F. Ji, Solid-liquid interfacial energy and melting properties of nickel under pressure from molecular dynamics, J. Chem. Eng. Data 55 (2010) 5149–5155. doi:https://doi.org/10.1021/je1007058.

[49] R. Hashimoto, Y. Shibuta, T. Suzuki, Estimation of solid-liquid interfacial energy from gibbs-thomson effect: A molecular dynamics study, ISIJ International 51 (2011) 1664–1667.

[50] J. J. Hoyt, M. Asta, A. Karma, Method for computing the anisotropy of the solid-liquid interfacial free energy, Phys. Rev. Lett. 86 (2001) 5530–5533. doi:10.1103/PhysRevLett.86.5530.

[51] K. Kelton, Crystal Nucleation in Liquids and Glasses, Vol. 45 of Solid State Physics, Academic Press, 1991. doi:https://doi.org/10.1016/S0081-1947(08)60144-7.

[52] N. Wu, X. Lu, R. An, X. Ji, Thermodynamic analysis and modification of gibbs–thomson equation for melting point depression of metal nanoparticles, Chinese Journal of Chemical Engineering 31 (2021) 198–205, frontiers of Chemical Engineering Thermodynamics. doi:https://doi.org/10.1016/j.cjche.2020.11.035.

[53] A. A. Wheeler, W. J. Boettinger, G. B. McFadden, Phase-field model for isothermal phase transitions in binary alloys, Phys. Rev. A 45 (1992) 7424–7439. doi:10.1103/PhysRevA.45.7424.

[54] S. Coriell, D. Turnbull, Relative roles of heat transport and interface rearrangement rates in the rapid growth of crystals in undercooled melts, Acta Metallurgica 30 (12) (1982) 2135–2139. doi:https://doi.org/10.1016/0001-6160(82)90134-1.

[55] Y. Wang, J. Shi, Y. Liu, Competitive grain growth and dendrite morphology evolution in selective laser melting of inconel 718 superalloy, Journal of Crystal Growth 521 (2019) 15–29.

[56] A. F. Ferreira, A. J. da Silva, J. A. de Castro, Simulation of the solidification of pure nickel via the phase-field method, Materials Research 9 (2006) 349–356.

[57] J. Warren, W. Boettinger, Prediction of dendritic growth and microsegregation patterns in a binary alloy using the phase-field method, Acta Metallurgica et Materialia 43 (2) (1995) 689–703.

[58] C.-A. Gandin, R. Schaefer, M. Rappaz, Analytical and numerical predictions of dendritic grain envelopes, Acta Materialia 44 (8) (1996) 3339–3347. doi:https://doi.org/10.1016/1359-6454(95)00433-5.

[59] S. Chen, G. Guillemot, C.-A. Gandin, Three-dimensional cellular automaton-finite element modeling of solidification grain structures for arc-welding processes, Acta Materialia 115 (2016) 448–467. `doi:https://doi.org/10.1016/j.actamat.2016.05.011`.

[60] J. A. Koepf, M. R. Gotterbarm, M. Markl, C. Körner, 3d multi-layer grain structure simulation of powder bed fusion additive manufacturing, Acta Materialia 152 (2018) 119–126. `doi:https://doi.org/10.1016/j.actamat.2018.04.030`.

[61] A. Baumard, D. Ayrault, O. Fandeur, C. Bordreuil, F. Deschaux-Beaume, Numerical prediction of grain structure formation during laser powder bed fusion of 316 l stainless steel, Materials & Design 199 (2021) 109434. `doi:https://doi.org/10.1016/j.matdes.2020.109434`.

[62] A. Pineau, G. Guillemot, D. Tourret, A. Karma, C.-A. Gandin, Growth competition between columnar dendritic grains – cellular automaton versus phase field modeling, Acta Materialia 155 (2018) 286–301. `doi:https://doi.org/10.1016/j.actamat.2018.05.032`.

[63] E. Dorari, K. Ji, G. Guillemot, C.-A. Gandin, A. Karma, Growth competition between columnar dendritic grains - the role of microstructural length scales, Acta Materialia (2021) 117395`doi:https://doi.org/10.1016/j.actamat.2021.117395`.

[64] P. Jácome, M. Fernandes, A. Garcia, A. Ferreira, J. de Castro, I. Ferreira, Application of computational thermodynamics to the evolution of surface tension and gibbs-thomson coefficient during multicomponent aluminum alloy solidification, Materials Science Forum 869 (2016) 416–422. `doi:https://doi.org/10.4028/www.scientific.net/msf.869.416`.

[65] D. J. S. Ferreira, B. N. Bezerra, M. N. Collyer, A. Garcia, I. L. Ferreira, The use of computational thermodynamics for the determination of surface tension and gibbs–thomson coefficient of multicomponent alloys jo - continuum mechanics and thermodynamics, Continuum Mechanics and Thermodynamics volume 30 (5) (2018) 1145–1154. `doi:https://doi.org/10.1007/s00161-018-0670-6`.

[66] W. J. Boettinger, S. R. Coriell, Microstructure formation in rapidly solidified alloys, Science and Technology of the Undercooled Melt, Sahm, P. R., H. Jones, and C. M. Adam (eds.) (1986) 81–109.

[67] M. J. Aziz, T. Kaplan, Continuous growth model for interface motion during alloy solidification, Acta Metallurgica 36 (8) (1988) 2335–2347. `doi:https://doi.org/10.1016/0001-6160(88)90333-1`.

[68] M. Hillert, Solute drag, solute trapping and diffusional dissipation of gibbs energy11this paper is based on the hume–rothery lecture presented at the 128th tms annual meeting, 1 march 1999, san diego, u.s.a., Acta Materialia 47 (18) (1999) 4481–4505. `doi:https://doi.org/10.1016/S1359-6454(99)00336-5`.

[69] S.-C. Huang, M. Glicksman, Fundamentals of dendritic solidification-i. steady-state tip growth, Acta Metallurgica 29 (5) (1981) 701–715.

[70] S.-C. Huang, M. Glicksman, Fundamentals of dendritic solidification-ii development of sidebranch structure, Acta Metallurgica 29 (5) (1981) 717–734.

[71] C. Gu, Y. Wei, F. Yu, X. Liu, L. She, Cellular Automaton Study of Hydrogen Porosity Evolution Coupled with Dendrite Growth During Solidification in the Molten Pool of Al-Cu Alloys, Metallurgical and Materials Transactions A 48 (2017) 4314–4323.

[72] R. Chen, Q. Xu, B. Liu, Cellular automaton simulation of three-dimensional dendrite growth in al–7si–mg ternary aluminum alloys, Computational Materials Science 105 (2015) 90–100. `doi:https://doi.org/10.1016/j.commatsci.2015.04.035`.

[73] J. W. Boettinger, The solidification of multicomponent alloys, Journal of Phase Equilibria and Diffusion 37 (1) (2016) 4–18. `doi:https://doi.org/10.1007/s11669-015-0416-0`.

[74] P. Carter, D. Cox, C.-A. Gandin, R. Reed, Process modelling of grain selection during the solidification of single crystal superalloy castings, Materials Science and Engineering: A 280 (2) (2000) 233–246. `doi:https://doi.org/10.1016/S0921-5093(99)00701-7`.

[75] P. Liu, Z. Wang, Y. Xiao, M. F. Horstemeyer, X. Cui, L. Chen, Insight into the mechanisms of columnar to equiaxed grain transition during metallic additive manufacturing, Additive Manufacturing 26 (2019) 22–29.

[76] P. Promoppatum, S.-C. Yao, P. C. Pistorius, A. D. Rollett, P. J. Coutts, F. Lia, R. Martukanitz, Numerical modeling and experimental validation of thermal history and microstructure for additive manufacturing of an inconel 718 product, Progress in Additive Manufacturing 3 (1) (2018) 15–32.

[77] D. M. Stefanescu, Science and Engineering of Casting Solidification 2nd ed., Springer, New York, NY., 2009.

[78] G. Guillemot, C.-A. Gandin, Analytical model for equiaxed globular solidification in multicomponent alloys, Acta

Materialia 97 (2015) 419–434. `doi:https://doi.org/10.1016/j.actamat.2015.04.030`.

[79] G. Guillemot, C.-A. Gandin, An analytical model with interaction between species for growth and dissolution of precipitates, Acta Materialia 134 (2017) 375–393. `doi:https://doi.org/10.1016/j.actamat.2017.04.035`.

[80] S. Coriell, R. Sekerka, Oscillatory morphological instabilities due to non-equilibrium segregation, Journal of Crystal Growth 61 (3) (1983) 499–508. `doi:10.1016/0022-0248(83)90179-3`.

[81] G. Merchant, S. Davis, Morphological instability in rapid directional solidification, Acta Metallurgica et Materialia 38 (12) (1990) 2683–2693. `doi:10.1016/0956-7151(90)90282-L`.

[82] J. Kittl, P. Sanders, M. Aziz, D. Brunco, M. Thompson, Complete experimental test of kinetic models for rapid alloy solidification, Acta Materialia 48 (20) (2000) 4797–4811. `doi:https://doi.org/10.1016/S1359-6454(00)00276-7`.

[83] S. Li, J. Zhang, P. Wu, Numerical solution and comparison to experiment of solute drag models for binary alloy solidification with a planar phase interface, Scripta Materialia 62 (9) (2010) 716–719. `doi:https://doi.org/10.1016/j.scriptamat.2010.01.041`.

[84] NIST, Physical Measurement Laboratory, Fundamental Physical Constants (2021).
URL `https://www.nist.gov/pml/fundamental-physical-constants`

[85] W. Kurz, R. Trivedi, Banded solidification microstructures, Metallurgical and Materials Transactions A 27 (3) (1996) 625–634. `doi:https://doi.org/10.1007/BF02648951`.

[86] A. Norman, K. Eckler, A. Zambon, F. Gärtner, S. Moir, E. Ramous, D. Herlach, A. Greer, Application of microstructure-selection maps to droplet solidification: a case study of the ni–cu system, Acta Materialia 46 (10) (1998) 3355–3370. `doi:https://doi.org/10.1016/S1359-6454(98)00078-0`.

[87] D. M. Herlach, Non-equilibrium solidification of undercooled metallic melts, Metals 4 (2) (2014) 196–234. `doi:https://doi.org/10.3390/met4020196`.

[88] D. M. Herlach, S. Burggraf, P. Galenko, C.-A. Gandin, A. Garcia-Escorial, H. Henein, C. Karrasch, A. Mullis, M. Rettenmayr, J. Valloton, Solidification of Undercooled Melts of Al-Based Alloys on Earth and in Space, JOM 69 (8) (2017) 1303–1310. `doi:https://doi.org/10.1007/s11837-017-2402-y`.

[89] J. Strößner, M. Terock, U. Glatzel, Mechanical and microstructural investigation of nickel-based superalloy in718 manufactured by selective laser melting (slm), Advanced Engineering Materials 17 (8) (2015) 1099–1105. `doi:https://doi.org/10.1002/adem.201500158`.

[90] E. Liverani, S. Toschi, L. Ceschini, A. Fortunato, Effect of selective laser melting (SLM) process parameters on microstructure and mechanical properties of 316L austenitic stainless steel, Journal of Materials Processing Technology 249 (2017) 255–263. `doi:https://doi.org/10.1016/j.jmatprotec.2017.05.042`.